

ForgeryVCR: Visual-Centric Reasoning via Efficient Forensic Tools in MLLMs for Image Forgery Detection and Localization

Youqi Wang^{1,2*} [†] Shen Chen^{2*} [♣] Huawei Wang² Rongxuan Peng¹ Taiping Yao² Shunquan Tan¹ [✉]
 Changsheng Chen¹ Bin Li¹ Shouhong Ding² [✉]

Abstract

Existing Multimodal Large Language Models (MLLMs) for image forgery detection and localization predominantly operate under a text-centric Chain-of-Thought (CoT) paradigm. However, forcing these models to textually characterize imperceptible low-level tampering traces inevitably leads to hallucinations, as linguistic modalities are insufficient to capture such fine-grained pixel-level inconsistencies. To overcome this, we propose ForgeryVCR, a framework that incorporates a forensic toolbox to materialize imperceptible traces into explicit visual intermediates via Visual-Centric Reasoning. To enable efficient tool utilization, we introduce a Strategic Tool Learning post-training paradigm, encompassing gain-driven trajectory construction for Supervised Fine-Tuning (SFT) and subsequent Reinforcement Learning (RL) optimization guided by a tool utility reward. This paradigm empowers the MLLM to act as a proactive decision-maker, learning to spontaneously invoke multi-view reasoning paths including local zoom-in for fine-grained inspection and the analysis of invisible inconsistencies in compression history, noise residuals, and frequency domains. Extensive experiments reveal that ForgeryVCR achieves state-of-the-art (SOTA) performance in both detection and localization tasks, demonstrating superior generalization and robustness with minimal tool redundancy. The project page is available at <https://youqiwong.github.io/projects/ForgeryVCR/>.

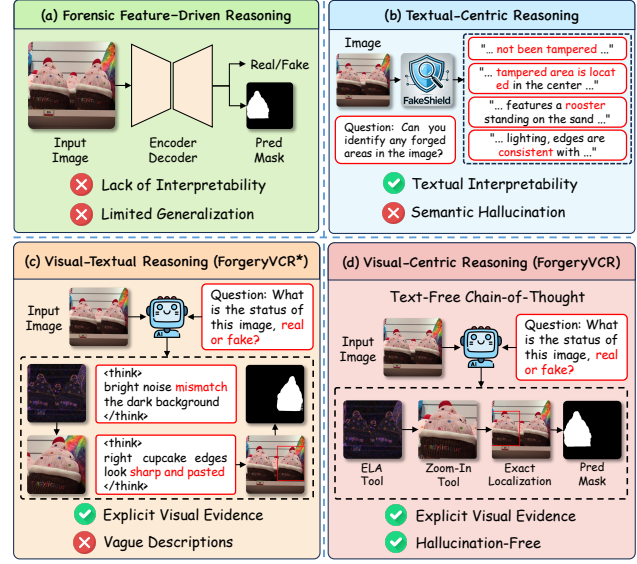


Figure 1. Motivation. Unlike prior methods limited by semantic bias, ForgeryVCR employs **Visual-Centric Reasoning**, grounding the verdict in visual evidence rather than vague descriptions.

1. Introduction

The rapid evolution of editing tools has created a deluge of hyper-realistic forgeries, establishing Image Forgery Detection and Localization (IFDL) as a crucial defense. Deep learning approaches predominantly capture subtle traces via frequency volumetric representations (Kwon et al., 2022), noise degradation modeling (Wu et al., 2022), or semantic-noise decoupling (Dong et al., 2023; Han et al., 2024). Advanced methods further employ learned noise fingerprints (Guillaro et al., 2023), sequential decision-making (Peng et al., 2024), masked attention (Kong et al., 2025), or adapted vision foundation models (Kwon et al., 2025; Peng et al., 2025). However, these specialized networks operate as black boxes lacking interpretability and generalization, as illustrated in Fig. 1(a).

To bridge interpretability and generalization gaps, recent efforts have shifted toward Multimodal Large Language Models (MLLMs). Forensic adaptations (Liu et al., 2025; Xu et al., 2025b; Lin et al., 2025a; Huang et al., 2025; Lin

*Equal contribution. [♣]Project Leader. [✉]Corresponding author.
[†]Work done during internship at Tencent YouTu Lab. ¹Shenzhen University ²Tencent YouTu Lab. Correspondence to: Shunquan Tan <tanshunquan@gmail.com>, Shouhong Ding <eric-shd@tencent.com>.

et al., 2025b) extend MLLMs to image forgery analysis by exploiting high-level semantic knowledge. However, these approaches face two critical limitations: 1) **Semantic Hallucinations.** Existing methods rely on a text-centric Chain-of-Thought (CoT) paradigm, yet linguistic modalities inherently suffer from information loss. As visualized in Fig. 1(b), linguistic descriptions fail to accurately align with specific tampering clues, inevitably leading to hallucinations where irrelevant scene context is misidentified as forgery evidence. 2) **Insensitivity to Low-Level Artifacts.** While low-level features have proven effective in traditional solutions, current MLLM architectures focus solely on high-level semantic extraction. This inherent bias renders them insensitive to low-level forensic information, limiting their ability to perceive subtle manipulation traces.

To mitigate the discrepancy between high-level semantics and low-level forensic artifacts, we introduce **ForgeryVCR**, a framework that employs Visual-Centric Reasoning. We reformulate the MLLM as a proactive decision-maker rather than a passive classifier, empowering it to plan, execute, and revise the forensic analysis. To substantiate this reasoning process, we equip the model with a Hybrid Forensics Toolbox via lightweight code execution. This toolbox integrates a zoom-in mechanism for fine-grained inspection alongside specialized operators spanning spatial, frequency, and noise domains, materializing imperceptible statistical inconsistencies into explicit visual intermediates. As illustrated in Fig. 1(c), our preliminary investigation indicates that vague textual interpretations of forensic patterns tend to misguide the decision-making. To rectify this, ForgeryVCR adopts the Visual-Centric Reasoning paradigm shown in Fig. 1(d). This framework eliminates the interference of ambiguous descriptions and directly derives the final decision from the explicitly generated visual intermediates, thereby achieving superior generalization in both forgery detection and localization tasks.

Our main contributions are summarized as follows:

- We introduce ForgeryVCR, the first framework in the IFDL domain to implement **Visual-Centric Reasoning** via forensic analysis tools. Our work reveals that this paradigm significantly outperforms models relying on textual explanations in capturing subtle manipulation traces, effectively mitigating hallucinations caused by semantic over-reliance.
- We propose an efficient tool utilization strategy to capture low-level artifacts essential for forensics. By employing **gain-driven tool selection** during SFT to construct effective reasoning trajectories, followed by RL optimization with a **tool utility reward**, we empower the MLLM to spontaneously invoke tools only when they yield decisive visual evidence.

- Extensive experiments demonstrate that ForgeryVCR achieves SOTA detection and localization performance with superior generalization across diverse benchmarks. Furthermore, our method exhibits exceptional robustness against real-world image degradations.

2. Related Work

2.1. Image Forgery Detection and Localization

Mainstream approaches for Image Forgery Detection and Localization (IFDL) can be broadly categorized into deep learning-based specialist networks and Multimodal Large Language Model (MLLM) adaptations.

Deep Learning-based Approaches. Traditional deep forensic networks operate as specialized experts designed to scrutinize low-level statistical anomalies. To capture invisible traces, methods like CAT-Net (Kwon et al., 2022) and IF-OSN (Wu et al., 2022) utilize dual-stream architectures or noise-aware schemes to analyze frequency domains and noise residuals. Moving towards fusing semantics with physical traces, TruFor (Guillaro et al., 2023) and MVSS-Net (Dong et al., 2023) combine learned noise fingerprints with edge supervision to model boundary discontinuities. Recent advancements further refine localization precision by synergizing RGB features with steganalysis models (HDF-Net (Han et al., 2024)), employing sequential decision-making (CoDE (Peng et al., 2024)), or utilizing advanced segmentation designs (PIM (Kong et al., 2025), SAFIRE (Kwon et al., 2025)).

MLLM-based Approaches. To address the interpretability and generalization issues of specialized networks, recent research has pivoted towards adapting MLLMs for forensics. ForgeryGPT (Liu et al., 2025) employs a three-stage training paradigm, introducing a mask-aware forgery extractor to explicitly align fine-grained tampering traces with linguistic features. Similarly, FakeShield (Xu et al., 2025b) utilizes a domain-tag generator and a tamper comprehension module to bridge the gap between semantic understanding and pixel-level localization for explainable diagnosis. SIDA (Huang et al., 2025) extends MLLM capabilities to social media deepfakes by incorporating specialized detection and segmentation tokens to unify authenticity assessment with mask generation. To address the lack of fine-grained perception in MLLMs, ProposeAndRectify (Zhang et al., 2025a) explicitly introduces low-level forensic information into the reasoning loop, employing a rectification module to validate semantic proposals using multi-scale physical artifacts.

Limitations. Despite their respective successes, both paradigms face inherent challenges. Specialized deep networks fundamentally operate as black boxes; they lack interpretability and suffer from poor generalization against novel attacks due to their reliance on fixed feature distributions.

Conversely, while MLLM-based approaches offer better explainability, they heavily prioritize high-level semantics. This text-centric bias often leads to hallucinations driven by scene context, as the models struggle to explicitly ground their reasoning in subtle low-level forensic artifacts.

2.2. Visual Chain-of-Thought

The paradigm of Chain-of-Thought (CoT) has recently evolved from textual reasoning to the multimodal domain, aiming to bridge the gap between visual perception and logical deduction. Recent studies unifiedly interpret this as integrating intermediate visual representations into the reasoning chain (Cheng et al., 2025). In contrast to text-centric paradigms which rely solely on linguistic rationales, visual-interleaved strategies explicitly generate or retrieve visual evidence to ground the reasoning process.

To implement such active perception, pioneering works have introduced the thinking with images paradigm. Methods like Chain-of-Focus (CoF) (Zhang et al., 2025b) and Deep-Eyes (Zheng et al., 2025) empower MLLMs to perform adaptive visual search by iteratively zooming in on key image regions, employing reinforcement learning to optimize the focus trajectory. Similarly, VCTP (Chen et al., 2024) proposes a see-think-confirm cycle to iteratively verify visual concepts against external knowledge. Beyond spatial attention, recent approaches integrate broader visual operations; for instance, VACoT (Xu et al., 2025a) utilizes post-hoc visual augmentations (e.g., denoising, rotation) to enhance robustness against adversarial OCR samples, while DeepEyesV2 (Hong et al., 2025) unifies code execution and web search to handle complex real-world queries.

However, adapting these general frameworks to IFDL presents unique challenges. Even equipped with general visual processing tools, the visual encoders of MLLMs remain fundamentally blind to imperceptible forensic artifacts that lie beyond dominant semantic content. Moreover, current MLLMs lack the intrinsic capability to dynamically and efficiently invoke the appropriate tools. To bridge this gap, our ForgeryVCR repurposes the Visual-CoT paradigm for the forensic domain. We integrate specialized tools capable of exposing low-level visual patterns and employ a gain-driven mechanism to ensure strategic and efficient tool invocation. This establishes a framework of Visual-Centric Reasoning, enabling the model to ground its judgment in explicit visual evidence rather than vague semantic biases.

3. Methodology

We begin by outlining the overall architecture and the investigative workflow in Section 3.1. Subsequently, Section 3.2 details the hybrid forensics toolbox utilized to expose imperceptible artifacts. Section 3.3 introduces the trajectories syn-

thesis pipeline, incorporating Gain-Driven Tool Selection and Multi-Trajectories Diversification. Finally, Section 3.4 describes the Strategic Tool Learning Pipeline, comprising SFT and RL via Group Relative Policy Optimization (GRPO) (Guo et al., 2025) to foster strategic tool usage.

3.1. Architecture

ForgeryVCR establishes a Visual-Centric Reasoning architecture. In this paradigm, the MLLM functions as a proactive agent that constructs a reasoning chain grounded in explicit forensic mappings. Crucially, this design bypasses the reliance on linguistic descriptors, enabling the model to directly perceive and process the generated visual outputs to expose hidden manipulation artifacts.

As illustrated in Fig. 2, the inference workflow begins with a preliminary visual assessment. When the initial evidence is ambiguous, the model dynamically invokes specific tools from the hybrid forensics toolbox. These tools materialize latent artifacts into discernible visual cues, which are then re-injected into the context window to ground the reasoning process. Upon concluding the investigation with a forgery verdict, the model predicts a bounding box to localize the manipulated region. Finally, to ensure pixel-level precision, we feed this bounding box as a visual prompt into the Segment Anything Model 2 (SAM2) (Ravi et al., 2024), directly generating a high-quality segmentation mask.

3.2. Hybrid Forensics Toolbox

To bridge the perceptual gap in MLLMs for image forgery analysis, we introduce the Hybrid Forensics Toolbox designed to materialize imperceptible artifacts into explicit visual evidence. Although numerous forensic tools exist across spatial, frequency, and generative domains (as detailed in Appendix C.1), integrating them indiscriminately proves suboptimal. Our preliminary analysis indicates that significant feature redundancy exists among these tools, where stacking excessive operators leads to performance saturation rather than linear improvement. As evidenced by the quantitative analysis in Table 11, adding redundant operators introduces unnecessary complexity to the tool selection policy without yielding tangible benefits. Therefore, we strategically select a sufficient set of tools that exhibit strong complementarity and necessity. This selection ensures the comprehensive capture of diverse manipulation traces while maintaining an efficient decision space.

Forensic Analysis Tools. We integrate three representative forensic algorithms to convert invisible statistical inconsistencies into distinct visual maps that the MLLM can directly perceive: (1) **Error Level Analysis (ELA):** This tool (Lu et al., 2025) visualizes discrepancies in compression levels. It highlights regions with different compression

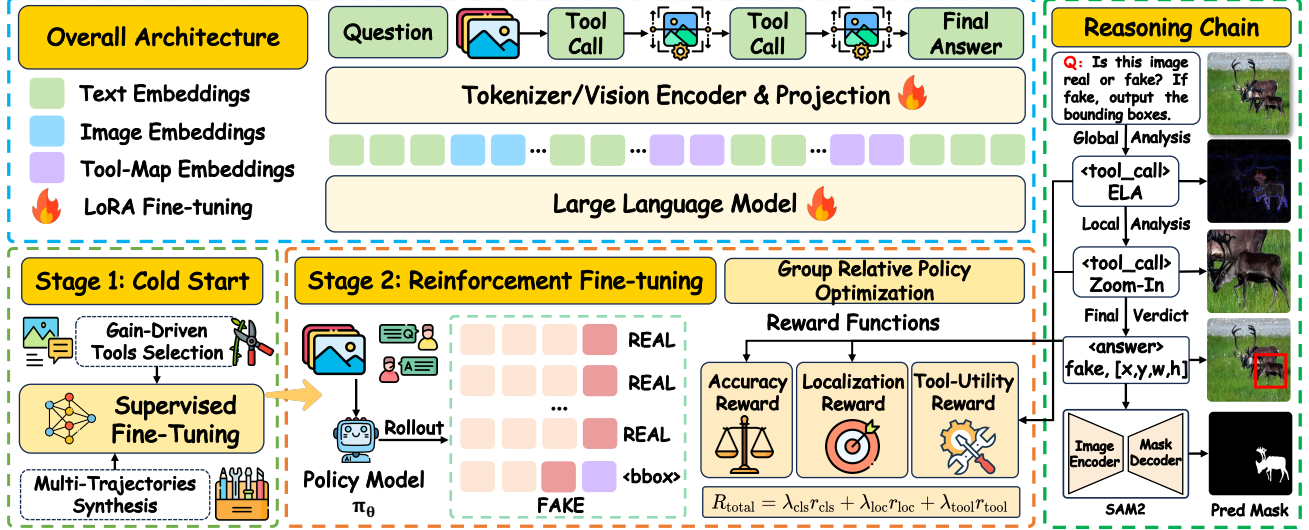


Figure 2. Overview of the ForgeryVCR Framework. The top panel depicts the architecture. The training pipeline: (1) Stage 1 uses Gain-Driven Tool Selection and Multi-Trajectories Synthesis to construct diverse reasoning paths; (2) Stage 2 optimizes the policy via GRPO with Tool-Utility Reward to foster strategic tool usage. The right panel shows the reasoning chain invoking tools to expose subtle artifacts for precise localization, guiding SAM2 to generate the fine-grained mask.

histories as distinct high-response areas compared to the background. (2) **Noise Print++ (NPP)**: This tool (Guillaro et al., 2023) extracts camera model fingerprints by analyzing noise residuals. It effectively reveals manipulation traces where the original sensor noise pattern is disrupted or inconsistent. (3) **Fast Fourier Transform (FFT)**: This tool (Kashiani et al., 2025) transforms the spatial signal into the frequency spectrum. It is particularly effective at exposing grid-like artifacts and spectral anomalies introduced by resampling and interpolation, providing complementary frequency-domain clues distinct from spatial features.

Visual Refinement Tool. Identifying tampering artifacts that occupy only a small proportion of the image requires fine-grained visual perception. However, under global scale perception, such subtle traces are often overwhelmed by global image context, making them difficult to distinguish reliably. To address this challenge, we introduce a Zoom-In mechanism for coarse to fine inspection. Upon identifying a suspicious area, the model extracts the corresponding region of interest for focused analysis. This strategy enables focused local perception, allowing the visual encoder to inspect pixel level details and manipulation traces.

3.3. Visual-Centric Trajectory Construction

Constructing high-quality reasoning trajectories is pivotal for aligning semantic understanding with forensic execution. Indiscriminate training on all available tools often leads to redundancy and inefficient tools dependency. To address this, we introduce a trajectory synthesis pipeline, as illustrated in Fig. 3, which rigorously filters effective tools and

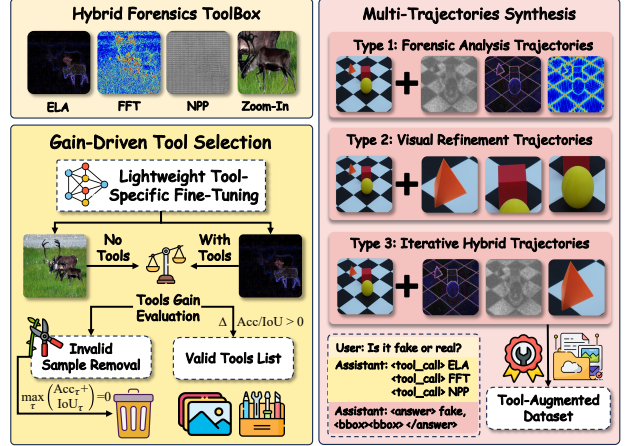


Figure 3. Pipeline of Visual-Centric Trajectory Construction.

generates diverse reasoning paths. This design ensures the model invokes forensic analysis and visual refinement tools only when they yield tangible information gains.

Gain-Driven Tool Selection. To mitigate redundancy induced by indiscriminate tool usage, we establish a mechanism to identify forensic operations yielding tangible gain. We begin with Lightweight Tool-Specific Fine-Tuning on the Cold-Start training set (details in Appendix D.1), where a tool-free baseline and independent single-tool models are trained without textual CoT. Subsequently, we execute Intractable Sample Removal (ISR) based on the inference results, filtering out samples where all models fail to yield correct classification or valid localization.

For the remaining diagnosable instances, we construct a sample-specific gain-driven set T_{valid} by identifying candidate tools from the pool T_{pool} that demonstrate superior performance over the tool-free baseline. We quantify the gain using a metric P conditioned on the sample type: it denotes the localization IoU for manipulated images and the normalized probability of the ground-truth class token for authentic ones. With the baseline performance P_{base} and a validity threshold τ , the selection criterion is formulated as:

$$T_{valid} = \{t \in T_{pool} \mid P_t > \max(P_{base}, \tau)\} \quad (1)$$

To enable gain-prioritized reasoning, we derive the final tool chain $T_{rank} = [t_1, \dots, t_M]$ by sorting the selected tools in descending order of their performance gain. Notably, if no tool surpasses the baseline (implying $T_{valid} = \emptyset$), T_{rank} remains empty, directing the model to perform direct visual assessment without tool invocation. The complete data construction procedure is outlined in Algorithm 1.

Multi-Trajectories Synthesis. Relying solely on a fixed trajectory prevents the MLLM from adaptively adjusting its tool invocation strategy based on sample complexity, often leading to the loss of direct visual assessment capabilities. To overcome this limitation, we employ a *Multi-Trajectory Synthesis (MTS)* strategy based on the ranked sequence T_{rank} . To ensure data balance during SFT, we truncate T_{rank} to the top- K candidates. We then construct the augmented reasoning set P_{aug} by unifying direct judgment, independent checks, and accumulative evidence:

$$P_{aug} = \underbrace{\{\emptyset\}}_{\text{No-Tool}} \cup \underbrace{\{[t_i]\}_{i=1}^{K'}}_{\text{Single-Tool}} \cup \underbrace{\{[t_1, \dots, t_k]\}_{k=2}^{K'}}_{\text{Multi-Tools}} \quad (2)$$

where $K' = \min(|T_{rank}|, K)$. The specific selection of K and the detailed synthesis algorithm are provided in Appendix D.1.

3.4. Strategic Tool Learning Pipeline

SFT-based Cold Start. To instantiate the visual-centric reasoning capability, we perform SFT using the structured trajectory dataset P_{aug} constructed in Sec. 3.3. The primary objective of this stage is to instill the fundamental protocol of Visual-CoT, aligning the model with the correct syntax for tool invocation and the sequential logic of visual evidence accumulation. We model this as a standard autoregressive generation task minimizing the cross-entropy loss:

$$\mathcal{L}_{SFT} = -\mathbb{E}_{(V, X, Y) \sim P_{aug}} \sum_{t=1}^T \log \pi_\theta(y_t \mid V, X, y_{<t}) \quad (3)$$

where π_θ denotes the policy, (V, X, Y) represent the visual input, textual instruction, and target response, and T is the sequence length.

Reinforcement Learning Optimization. While SFT ensures structural formatting, the MLLM often lacks adaptive tool selection and genuine perceptual grounding. To bridge this gap, we employ RL via GRPO to optimize the policy. For each query q , we sample a group of G outputs $\{o_i\}_{i=1}^G$ from the old policy $\pi_{\theta_{old}}$. The objective maximizes the advantage-weighted likelihood while constraining deviation from the reference policy π_{ref} :

$$\mathcal{J}(\theta) = \mathbb{E}_q \left[\frac{1}{G} \sum_{i=1}^G (\mathcal{L}_{clip}(o_i, A_i) - \beta \mathbb{D}_{KL}(\pi_\theta \parallel \pi_{ref})) \right] \quad (4)$$

where \mathcal{L}_{clip} denotes the clipped surrogate loss and β controls the KL penalty. Crucially, GRPO computes the advantage A_i by normalizing the total reward R_i within the group: $A_i = (R_i - \text{mean}(R)) / \text{std}(R)$. The reward R_i employs a composite function to guide forensic rigorosity, comprising three components: 1) **Classification Reward** (R_{cls}): We reward correct classification of the image. 2) **Localization Reward** (R_{loc}): We reward precise localization using the Intersection-over-Union (IoU) between predicted and ground-truth bounding boxes. 3) **Tool Utility Reward** (R_{tool}): we foster efficient execution by granting rewards only when tool invocation leads to correct classification or accurate localization.

The total reward is calculated as follows:

$$R_{total} = \lambda_{cls} R_{cls} + \lambda_{loc} R_{loc} + \lambda_{tool} R_{tool} \quad (5)$$

where each λ denotes a hyperparameter controlling the weight of the corresponding objective. Specific parameter settings are detailed in Appendix E.

4. Experiments

4.1. Experimental Setup

Baselines. To evaluate the efficacy of ForgeryVCR, we compare against three categories: 1) SOTA Traditional IFDL Methods. We select representative models focusing on low-level features, including MVSS-Net (Dong et al., 2023), IF-OSN (Wu et al., 2022), TruFor (Guillaro et al., 2023), CoDE (Peng et al., 2024), HDF-Net (Han et al., 2024), PIM (Kong et al., 2025), and SAFIRE (Kwon et al., 2025). 2) Forensic-tuned MLLM methods. We compare against emerging MLLMs adapted for forensics, namely FakeShield (Xu et al., 2025b) and SIDA (Huang et al., 2025). To ensure reproducibility, all selected methods have publicly available code or weights. 3) General-purpose MLLMs. As detailed in Section 4.4, we further include leading open-source MLLMs fine-tuned on the same protocol.

Datasets. Our experimental setup adopts distinct datasets for training and evaluation. The training procedure follows

a two-stage strategy, including SFT and RL. During SFT, we use the CASIA v2 dataset (Dong et al., 2013) with balanced authentic and tampered samples. In the RL stage, we further incorporate IMD2020 (Novozamsky et al., 2020) and a subset of FantasticReality (Kniaz et al., 2019). Detailed data composition for each stage and a comparison of training data scales with other methods, are provided in the Appendix B. Notably, the overall training data scale of ForgeryVCR is substantially smaller than that of most specialist forensic models and existing MLLM-based approaches.

We evaluate generalization on benchmarks including CASIA v1 (Dong et al., 2013), Columbia (Hsu & Chang, 2006), Coverage (Wen et al., 2016), CocoGlide (Guillaro et al., 2023), DSO (De Carvalho et al., 2013), Korus (Korus & Huang, 2017), In-the-wild (Huh et al., 2018), and NIST16 (Guan et al., 2019). These datasets cover diverse manipulation types, including copy-move, splicing, object removal, and AIGC-based inpainting.

Evaluation Metrics. To ensure a fair and standardized comparison, we strictly adhere to the evaluation protocols established in FakeShield (Xu et al., 2025b). For image-level forgery detection, we report the standard Accuracy (ACC) and F1-score. For traditional forensic networks that generate continuous probability maps, we apply a fixed threshold of 0.5 to binarize, classifying an image as tampered if it contains any positive pixels. For pixel-level localization, we employ the F1-score and Intersection over Union (IoU).

4.2. Image Forgery Detection Evaluation

Table 1 presents the quantitative comparison for image-level forgery detection. ForgeryVCR achieves SOTA performance, attaining a weighted average F1-score of 0.8271 and Accuracy of 0.8261. Compared to the second-best method, FakeShield, ForgeryVCR yields an absolute improvement of approximately 11%, with significant margins on challenging benchmarks such as Coverage and NIST16. Furthermore, the visual-centric approach consistently outperforms the visual-textual counterpart (ForgeryVCR*), demonstrating that bypassing linguistic descriptions mitigates semantic hallucinations and enhances detection accuracy. Notably, while pure localization methods attain perfect scores on the all-manipulated In-the-wild dataset, their low accuracy on balanced benchmarks exposes a severe false-positive bias, whereas ForgeryVCR maintains consistent metrics across diverse datasets, confirming superior generalization.

4.3. Image Forgery Localization Evaluation

Beyond detection, we evaluate pixel-level localization performance in Table 2. By utilizing the SAM2 with predicted bounding boxes as visual prompts, ForgeryVCR attains superior localization capabilities, recording an overall IoU

of 0.5306. The performance advantage over ForgeryVCR* underscores that the purely Visual-Centric Reasoning mechanism is essential for high-precision localization, as the inclusion of textual rationales tends to dilute the spatial exactness required for guiding segmentation. Consequently, our method achieves competitive performance against specialist networks. While specialist networks often exhibit domain-specific variances, ForgeryVCR delivers superior overall performance across diverse manipulation types. Additionally, our framework achieves leading performance in region-level localization, and we provide comprehensive BBox-IoU comparisons in Appendix F.4.

4.4. Comparison with General MLLMs

To benchmark against general-purpose architectures, we fine-tune representative open-source MLLMs using the identical dataset and pipeline detailed in Table 14. Crucially, these baselines are evaluated in a tool-free setting without utilizing visual-centric reasoning steps. To ensure consistency, we enforce a unified evaluation pipeline where SAM2 is utilized to generate segmentation masks from predicted bounding boxes, strictly adhering to the protocols in Table 1 and Table 2. As shown in Table 3, general MLLMs exhibit a distinct deficit compared to ForgeryVCR. This gap stems from standard pre-training prioritizing high-level semantics over the high-frequency sensitivity required for forensics. Consequently, straightforward fine-tuning is insufficient, confirming the necessity of integrating forensic tools.

4.5. Ablation Studies

Impact of Training Stages. Table 4 delineates the contribution of each training phase. The initial SFT stage significantly bridges the domain gap observed in the zero-shot baseline. Within this phase, both *Multi-Trajectories Synthesis (MTS)* and *Intractable Sample Removal (ISR)* prove essential. Their removal leads to a noticeable decline in performance, validating the need for diverse trajectories and high-quality training data. Most importantly, the subsequent RL stage yields the most substantial gains. This confirms that reward-driven policy optimization effectively refines the decision boundary and localization precision.

Impact of Reasoning Strategies. Table 5 compares distinct reasoning paradigms. The results show that Visual-CoT significantly boosts image-level Accuracy from 0.7561 to 0.8261 compared to the baseline. This improvement indicates that explicitly materializing forensic artifacts into visual intermediate steps is essential for capturing subtle manipulation traces. In contrast, the inclusion of Textual-CoT results in performance degradation across both detection and localization tasks. This suggests that intermediate linguistic rationales introduce hallucinations, whereas direct visual alignment offers superior precision for forensic analysis.

Table 1. Quantitative comparison of image-level forgery detection performance (F1 and Accuracy). Methods are separated by category (Specialist vs. MLLMs methods). Best and second-best results are marked in **bold** and underlined, respectively. The method marked with * denotes ForgeryVCR evaluated with visual and textual CoT. The column “Weighted Avg.” denotes the weighted average performance.

Method	CASIA v1		Coverage		CocoGlide		NIST16		Korus		DSO		Columbia		In-the-wild		Weighted Avg.	
	F1	ACC																
MVSS-Net (<i>TPAMI’22</i>)	0.7323	0.7599	0.6691	0.5500	0.6657	0.5605	0.5513	0.4167	0.6316	0.5386	0.6395	0.4700	0.7547	0.6777	0.9823	0.9652	0.6704	0.6017
IF-OSN (<i>CVPR’22</i>)	0.7127	0.6733	0.6596	0.5150	0.6205	0.5664	0.5634	0.4167	0.6688	0.5182	0.6667	0.5000	0.6742	0.5207	1.0000	1.0000	0.6582	0.5653
TruFor (<i>CVPR’23</i>)	0.7931	0.8105	0.5811	0.6900	0.4979	0.6436	0.5380	0.6708	0.4029	0.6227	0.9453	0.9450	0.9861	0.9862	0.7818	0.6418	0.6525	0.7350
CoDE (<i>TIFS’24</i>)	0.7043	0.5529	0.6689	0.5050	0.6675	0.5049	0.5660	0.4014	0.6656	0.5045	0.6667	0.5000	0.6679	0.5069	1.0000	1.0000	0.6645	0.5107
HDF-Net (<i>TPAMI’24</i>)	0.6886	0.5372	0.6688	0.5048	0.6654	0.5010	0.5501	0.3820	0.6627	0.4978	0.6667	0.5000	0.6800	0.5510	0.9976	<u>0.9952</u>	0.6619	0.5024
PIM (<i>TPAMI’25</i>)	0.7499	0.6948	0.6553	0.4950	0.6634	0.5244	0.5592	0.4153	0.6570	0.5159	0.6690	0.5250	0.6941	0.5702	0.9771	0.9552	0.6759	0.5655
SAFIRE (<i>AAAI’25</i>)	0.6937	0.5343	0.6645	0.5000	0.6671	0.5010	0.5629	0.3917	<u>0.6657</u>	0.5000	0.6688	0.5048	0.6654	0.5013	1.0000	1.0000	0.6602	0.5011
FakeShield (<i>ICLR’25</i>)	0.8800	0.8634	0.6048	0.5100	0.6684	0.5039	0.5895	0.6290	0.4693	0.5682	0.7063	0.6300	0.9202	0.9174	0.7855	0.6620	0.7172	0.6891
SIDA (<i>CVPR’25</i>)	0.5700	0.6366	0.0198	0.5050	0.6878	0.6621	0.2293	0.6292	0.1092	0.5182	0.0198	0.5050	0.8916	0.9008	0.8448	0.7313	0.4589	0.6412
ForgeryVCR*	0.8961	0.8953	0.7522	0.7200	0.7343	0.7314	0.6671	0.6688	0.6429	<u>0.6364</u>	0.7816	0.8100	0.8072	0.7631	0.9823	0.9652	0.7756	0.7711
ForgeryVCR	0.9193	0.9180	0.7963	0.7800	0.7835	0.7842	0.7271	0.7556	0.6284	0.6909	0.8497	<u>0.8550</u>	0.9045	0.8953	0.9719	0.9453	0.8271	0.8261

Table 2. Quantitative comparison of pixel-level forgery localization performance (F1 and IoU). Methods are separated by category (Specialist vs. MLLMs methods). Best and second-best results are marked in **bold** and underlined, respectively. The method marked with * denotes ForgeryVCR evaluated with visual and textual CoT. The column “Weighted Avg.” denotes the weighted average performance.

Method	CASIA v1		Coverage		CocoGlide		NIST16		Korus		DSO		Columbia		In-the-wild		Weighted Avg.	
	F1	IoU																
MVSS-Net (<i>TPAMI’22</i>)	0.4315	0.3792	0.4556	0.3788	0.3321	0.2563	0.3047	0.2476	0.1025	0.0752	0.2621	0.1839	0.6545	0.5554	0.2856	0.2158	0.3605	0.2989
IF-OSN (<i>CVPR’22</i>)	0.5089	0.4651	0.2660	0.1778	0.2639	0.2069	0.2695	0.1988	0.2984	0.2213	0.4205	0.2892	0.6856	0.5733	0.4965	0.3847	0.3979	0.3296
TruFor (<i>CVPR’23</i>)	0.6864	0.6228	0.5248	0.4508	0.3615	0.2935	0.3933	0.3170	0.3782	0.3016	0.9145	0.8669	0.7635	0.6882	0.6278	0.5356	0.5467	0.4761
CoDE (<i>TIFS’24</i>)	0.7232	0.6371	0.4638	0.3592	0.4887	0.3867	0.4220	0.3398	0.2780	0.2142	0.3767	0.2655	0.8922	0.8531	0.5598	0.4495	0.5620	0.4752
HDF-Net (<i>TPAMI’24</i>)	0.3421	0.2732	0.3613	0.2551	0.2960	0.2168	0.2948	0.2233	0.2391	0.1747	0.2914	0.1896	0.4801	0.4064	0.3880	0.2818	0.3271	0.2506
PIM (<i>TPAMI’25</i>)	0.5665	0.5122	0.2516	0.1885	0.4047	0.3271	0.2829	0.2278	0.2158	0.1603	0.2532	0.1949	0.5851	0.5122	0.4184	0.3382	0.4202	0.3579
SAFIRE (<i>AAAI’25</i>)	0.3345	0.2764	0.5757	0.5058	0.4710	<u>0.3983</u>	0.4177	0.3466	<u>0.3431</u>	0.2704	0.4578	0.3919	0.7520	0.7191	0.4578	0.3805	0.4257	0.3607
FakeShield (<i>ICLR’25</i>)	0.5940	0.5376	0.2418	0.2117	0.5205	0.4280	0.2598	0.2286	0.1251	0.1016	0.4450	0.4157	0.7440	0.6581	0.4781	0.4265	0.4597	0.4047
SIDA (<i>CVPR’25</i>)	0.2948	0.2510	0.2922	0.2257	0.4717	0.3816	0.3184	0.2644	0.1808	0.1346	0.1695	0.1309	0.4661	0.3944	0.4248	0.3414	0.3388	0.2790
ForgeryVCR*	0.6948	0.6399	0.6599	0.6174	0.4405	0.3714	0.5001	0.4555	0.3156	0.2682	0.5465	0.5157	0.8205	0.7601	0.6918	0.6130	<u>0.5805</u>	0.5249
ForgeryVCR	0.7092	0.6513	0.6732	0.6308	0.4560	0.3785	0.5001	<u>0.4554</u>	0.2717	0.2336	<u>0.6156</u>	<u>0.5753</u>	<u>0.8309</u>	0.7700	<u>0.6905</u>	0.6146	0.5881	0.5306

Table 3. Performance comparison of general MLLMs fine-tuned via the SFT and RL training pipeline. Best results are marked in **bold** and second-best are underlined.

Method	Detection		Localization	
	F1	ACC	F1	IoU
InternVL3.5-8B	0.6856	0.7105	0.3874	0.3482
Llama-3.2-11B-Vision	0.7085	0.7090	0.4575	0.4076
LLaVA-OneVision-1.5-8B	0.6671	0.5005	0.1711	0.1216
Qwen-3-VL-2B	0.7057	0.7568	0.4597	0.4218
Qwen-3-VL-4B	<u>0.7351</u>	0.7561	<u>0.4814</u>	<u>0.4357</u>
Qwen-3-VL-8B	0.7180	<u>0.7686</u>	0.4454	0.4053
ForgeryVCR	0.8271	0.8261	0.5881	0.5306

Impact of Reward Functions. Table 6 analyzes the contribution of distinct reward components. We observe that relying solely on the classification reward yields suboptimal localization, whereas adding the localization reward improves pixel-level metrics but degrades detection accuracy, indicating an optimization conflict. The integration of the Tool Utility Reward mitigates this issue by guiding strategic tool invocation. Consequently, the comprehensive reward formulation attains superior performance across all metrics, demonstrating that incentivizing efficient tool usage

Table 4. Ablation study on the effectiveness of training stages. Best results are marked in **bold** and second-best are underlined.

Method	Image-level Detection		Pixel-level Localization	
	F1	ACC	F1	IoU
Base Model	0.5200	0.6600	0.2193	0.2742
+ SFT	0.6289	0.5936	0.3948	0.3573
+ SFT + ISR	0.6499	0.6589	0.3953	0.3596
+ SFT + ISR + MTS	<u>0.6903</u>	<u>0.6893</u>	0.4464	0.4049
ForgeryVCR	0.8271	0.8261	0.5881	0.5306

effectively harmonizes the trade-off between global forgery detection and fine-grained forgery localization.

Impact of Toolbox Components. Table 7 evaluates the contribution of the toolbox components. We observe that utilizing Zoom-In mechanism alone yields inferior performance compared to forensic tools. Since MLLMs inherently lack perception of low-level statistical inconsistencies, mere visual magnification fails to capture imperceptible traces. Consequently, the substantial performance gain from their combination stems from the forensic tools’ ability to materialize imperceptible traces, directing the MLLM to suspicious regions for fine-grained inspection.

Table 5. Ablation study on the efficacy of different CoT modalities. Best results are marked in **bold** and second-best are underlined.

CoT Modality	Image-level Detection		Pixel-level Localization			
	Visual	Textual	F1	ACC	F1	IoU
✗	✗		0.7351	0.7561	0.4814	0.4357
✗	✓		0.6431	0.7215	0.4514	0.4107
✓	✓		<u>0.7756</u>	<u>0.7711</u>	<u>0.5805</u>	<u>0.5249</u>
✓	✗		0.8271	0.8261	0.5881	0.5306

Table 6. Ablation study on the impact of different reward components in the RL stage. Best results are marked in **bold** and second-best are underlined.

Reward Functions		Image-level Detection		Pixel-level Localization	
R_{cls}	R_{loc}	F1	ACC	F1	IoU
✓		<u>0.7891</u>	<u>0.7944</u>	0.5227	0.4688
✓	✓	0.7544	0.7339	<u>0.5554</u>	<u>0.5005</u>
✓	✓	0.8271	0.8261	0.5881	0.5306

Table 7. Ablation study on the contribution of tools in the toolbox. Best results are marked in **bold** and second-best are underlined.

Toolbox		Image-level Detection		Pixel-level Localization	
Forensics Tools	Zoom-In Tool	F1	ACC	F1	IoU
✓		<u>0.7342</u>	<u>0.7700</u>	<u>0.4843</u>	<u>0.4420</u>
	✓	0.7118	0.6981	0.4574	0.4099
✓	✓	0.8271	0.8261	0.5881	0.5306

4.6. Analysis

Training Dynamics. Fig. 4 tracks the evolution of model dynamics during the RL stage. The steady ascent in total reward contrasts with the stabilization of interaction turns at a lower level, indicating that the MLLM evolves from random exploration to adaptive execution. Crucially, this reduction in tool usage does not compromise performance; instead, it reflects a learned selectivity where the model invokes specific forensic tools only when necessary for the given input. This behavior confirms that reward-driven optimization fosters a task-aware strategy, effectively balancing detection precision with computational efficiency by eliminating redundant inference steps.

Tool Usage. We further analyze the distribution of tool invocations in Fig. 5 and Fig. 6 to evaluate the impact of reward-driven alignment. Initially, the SFT stage exhibits a tendency toward indiscriminate tool usage, notably applying the Zoom-In function frequently even on authentic images. In contrast, the RL stage effectively suppresses these non-informative invocations by optimizing for utility. As evidenced by the dataset-specific statistics, the MLLM learns to autonomously bypass tool invocation when direct visual assessment suffices, leading to a notable increase in direct inference across all benchmarks. This transition confirms that the model shifts from mechanical execution to a dynamic, efficiency-oriented investigation policy.

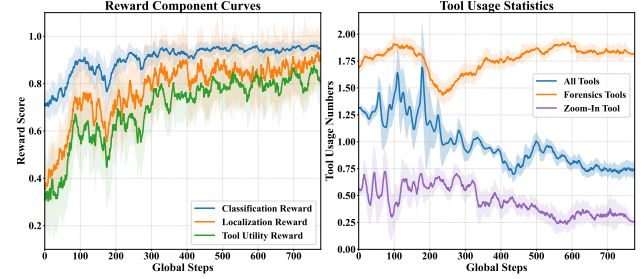


Figure 4. Evolution of training dynamics during the RL stage.

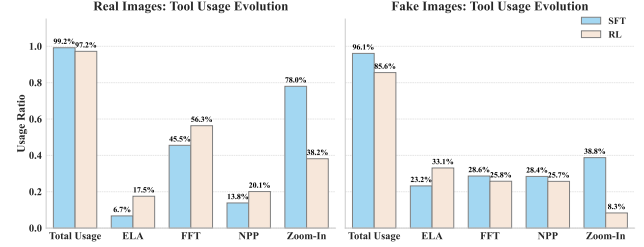


Figure 5. Comparison of specific tool usage ratios between SFT and RL stages.

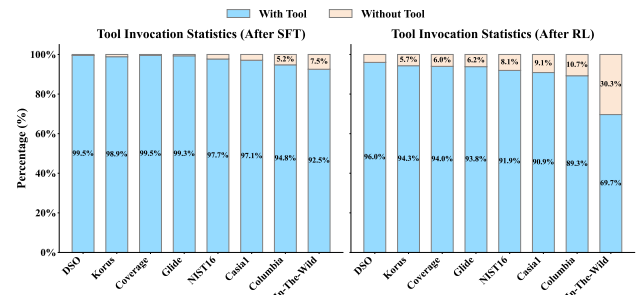


Figure 6. Evolution of tool usage ratios from SFT to RL stages across benchmarks.

5. Conclusion

In this paper, we propose ForgeryVCR, which establishes a Visual-Centric Reasoning paradigm to empower MLLMs with the capability to perceive imperceptible tampering traces. By converting statistical inconsistencies into explicit visual evidence, our approach effectively mitigates semantic hallucinations caused by linguistic descriptions. To ensure rigorous tool utilization, we introduce a Strategic Tool Learning pipeline. The gain-driven SFT stage constructs diverse reasoning trajectories to retain high-quality investigative paths, while the subsequent RL optimization, guided by a Tool Utility Reward, fosters an efficient execution policy that maximizes detection accuracy and localization precision. Extensive experiments demonstrate that ForgeryVCR achieves SOTA performance, exhibiting superior generalization and exceptional robustness against post-processing degradations.

References

Bai, S., Chen, K., Liu, X., Wang, J., Ge, W., et al. Qwen2.5-VL technical report. *arXiv preprint*, abs/2502.13923, 2025.

Chen, Z., Zhou, Q., Shen, Y., Hong, Y., Sun, Z., et al. Visual chain-of-thought prompting for knowledge-based visual reasoning. In *Proceedings of the AAAI Conference on Artificial Intelligence*, volume 38, pp. 1254–1262, 2024.

Cheng, Z., Chen, Q., Xu, X., Wang, J., Wang, W., et al. Visual Thoughts: A unified perspective of understanding multimodal chain-of-thought. *arXiv preprint*, abs/2505.15510, 2025.

De Carvalho, T. J., Riess, C., Angelopoulou, E., Pedrini, H., and de Rezende Rocha, A. Exposing digital image forgeries by illumination color classification. *IEEE Transactions on Information Forensics and Security*, 8(7):1182–1194, 2013.

Dong, C., Chen, X., Hu, R., Cao, J., and Li, X. MVSS-Net: Multi-view multi-scale supervised networks for image manipulation detection. *IEEE Transactions on Pattern Analysis and Machine Intelligence*, 45(3):3539–3553, March 2023. ISSN 1939-3539. doi: 10.1109/TPAMI.2022.3180556.

Dong, J., Wang, W., and Tan, T. Casia image tampering detection evaluation database. In *Proceedings of the 2013 IEEE China Summit and International Conference on Signal and Information Processing*, pp. 422–426, 2013.

Guan, H., Kozak, M., Robertson, E., Lee, Y., Yates, A. N., et al. MFC Datasets: Large-scale benchmark datasets for media forensic challenge evaluation. In *Proceedings of the IEEE/CVF Winter Conference on Applications of Computer Vision Workshops (WACVW)*, pp. 63–72, 2019.

Guillaro, F., Cozzolino, D., Sud, A., Dufour, N., and Verdoliva, L. TruFor: Leveraging all-round clues for trustworthy image forgery detection and localization. In *Proceedings of the IEEE/CVF Conference on Computer Vision and Pattern Recognition*, pp. 20606–20615, 2023.

Guo, D., Yang, D., Zhang, H., Song, J., Wang, P., et al. DeepSeek-R1 incentivizes reasoning in llms through reinforcement learning. *Nature*, 645(8081):633–638, 2025. doi: 10.1038/s41586-025-09422-z.

Han, R., Wang, X., Bai, N., Wang, Y., Hou, J., et al. HDF-Net: Capturing homogeny difference features to localize the tampered image. *IEEE Transactions on Pattern Analysis and Machine Intelligence*, 46(12):10005–10020, December 2024. ISSN 1939-3539. doi: 10.1109/TPAMI.2024.3432551.

Hong, J., Zhao, C., Zhu, C., Lu, W., Xu, G., et al. DeepEyesV2: Toward agentic multimodal model. *arXiv preprint*, abs/2511.05271, 2025.

Hsu, Y.-f. and Chang, S.-f. Detecting image splicing using geometry invariants and camera characteristics consistency. In *Proceedings of the IEEE International Conference on Multimedia and Expo (ICME)*, pp. 549–552, 2006.

Huang, Z., Hu, J., Li, X., He, Y., Zhao, X., et al. SIDA: Social media image deepfake detection, localization and explanation with large multimodal model. In *Proceedings of the IEEE/CVF Conference on Computer Vision and Pattern Recognition*, pp. 28831–28841, 2025.

Huh, M., Liu, A., Owens, A., and Efros, A. A. Fighting Fake News: Image splice detection via learned self-consistency. In *Proceedings of the European Conference on Computer Vision*, pp. 101–117, 2018.

Kashiani, H., Talemi, N. A., and Afghah, F. FreqDebias: Towards generalizable deepfake detection via consistency-driven frequency debiasing. In *Proceedings of the IEEE/CVF Conference on Computer Vision and Pattern Recognition*, pp. 8775–8785, June 2025.

Kniaz, V. V., Knyaz, V., and Remondino, F. The point where reality meets fantasy: Mixed adversarial generators for image splice detection. In *Advances in Neural Information Processing Systems*, volume 32, 2019.

Kong, C., Luo, A., Wang, S., Li, H., Rocha, A., et al. Pixel-inconsistency modeling for image manipulation localization. *IEEE Transactions on Pattern Analysis and Machine Intelligence*, 47(6):4455–4472, 2025.

Korus, P. and Huang, J. Multi-scale analysis strategies in PRNU-based tampering localization. *IEEE Transactions on Information Forensics and Security*, 12(4):809–824, 2017.

Kwon, M.-J., Nam, S.-H., Yu, I.-J., Lee, H.-K., and Kim, C. Learning JPEG compression artifacts for image manipulation detection and localization. *International Journal of Computer Vision*, 130(8):1875–1895, 2022.

Kwon, M.-J., Lee, W., Nam, S.-H., Son, M., and Kim, C. SAFIRE: Segment any forged image region. In *Proceedings of the AAAI Conference on Artificial Intelligence*, volume 39, pp. 4437–4445, April 2025. doi: 10.1609/aaai.v39i4.32467. URL <https://ojs.aaai.org/index.php/AAAI/article/view/32467>.

Lin, K., Yan, Z., Chen, R., Ye, J., Zhang, K.-Y., Zhou, Y., Jin, P., Li, B., Yao, T., and Ding, S. Seeing before reasoning: A unified framework for generalizable and explainable fake image detection. *arXiv preprint arXiv:2509.25502*, 2025a.

Lin, K., Yan, Z., Zhang, K.-Y., Hao, L., Zhou, Y., Lin, Y., Li, W., Yao, T., Ding, S., and Li, B. Guard Me If You Know Me: Protecting specific face-identity from deepfakes. *arXiv preprint arXiv:2505.19582*, 2025b.

Liu, J., Zhang, F., Zhu, J., Sun, E., Zhang, Q., et al. ForgeryGPT: Multimodal large language model for explainable image forgery detection and localization. *arXiv preprint, abs/2410.10238*, 2025.

Liu, X., Liu, Y., Chen, J., and Liu, X. PSCC-Net: Progressive spatio-channel correlation network for image manipulation detection and localization. *IEEE Transactions on Circuits and Systems for Video Technology*, 32(11):7505–7517, November 2022. ISSN 1558-2205. doi: 10.1109/TCSVT.2022.3189545.

Lu, X., Cheng, F., Luo, G., and Zhu, Y. MFDF-IML: Multi-feature dynamic fusion for image manipulation localization. In *Proceedings of the 28th International Conference on Computer Supported Cooperative Work in Design (CSCWD)*, pp. 686–691, 2025. doi: 10.1109/CSCWD64889.2025.11033390.

Novozamsky, A., Mahdian, B., and Saic, S. IMD2020: A large-scale annotated dataset tailored for detecting manipulated images. In *Proceedings of the IEEE/CVF winter conference on applications of computer vision workshops*, pp. 71–80, 2020.

Peng, R., Tan, S., Mo, X., Li, B., and Huang, J. Employing reinforcement learning to construct a decision-making environment for image forgery localization. *IEEE Transactions on Information Forensics and Security*, 19:4820–4834, 2024. ISSN 1556-6021. doi: 10.1109/TIFS.2024.3381470.

Peng, R., Tan, S., Kong, C., Luo, A., Kot, A. C., et al. ForensicsSAM: Toward robust and unified image forgery detection and localization resisting to adversarial attack. *arXiv preprint, abs/2508.07402*, 2025.

Ravi, N., Gabeur, V., Hu, Y.-T., Hu, R., Ryali, C., et al. SAM 2: Segment anything in images and videos. *arXiv preprint, abs/2408.00714*, 2024.

Su, Y., Tan, S., and Huang, J. A novel universal image forensics localization model based on image noise and segment anything model. In *Proceedings of the ACM Workshop on Information Hiding and Multimedia Security*, pp. 149–158, 2024. doi: 10.1145/3658664.3659639. URL <https://doi.org/10.1145/3658664.3659639>.

Su, Z., Li, L., Song, M., Hao, Y., Yang, Z., et al. Open-ThinkIMG: Learning to think with images via visual tool reinforcement learning. *arXiv preprint, 2025*. URL <https://arxiv.org/abs/2505.08617>.

Wang, H., Su, A., Ren, W., Lin, F., and Chen, W. Pixel Reasoner: Incentivizing pixel-space reasoning with curiosity-driven reinforcement learning. *arXiv preprint, 2025*. URL <https://arxiv.org/abs/2505.15966>.

Wang, Z., Bao, J., Zhou, W., Wang, W., Hu, H., et al. DIRE for diffusion-generated image detection. In *Proceedings of the IEEE/CVF International Conference on Computer Vision*, pp. 22445–22455, October 2023.

Wen, B., Zhu, Y., Subramanian, R., Ng, T.-T., Shen, X., et al. COVERAGE – A novel database for copy-move forgery detection. In *Proceedings of the IEEE International Conference on Image Processing (ICIP)*, pp. 161–165, 2016.

Wu, H., Zhou, J., Tian, J., and Liu, J. Robust image forgery detection over online social network shared images. In *Proceedings of the IEEE/CVF Conference on Computer Vision and Pattern Recognition*, pp. 13430–13439, 2022. doi: 10.1109/CVPR52688.2022.01308.

Xu, Z., Sun, C., Du, S., Li, C., Lyu, J., et al. VACoT: Rethinking visual data augmentation with vlms. *arXiv preprint, abs/2512.02361*, 2025a.

Xu, Z., Zhang, X., Li, R., Tang, Z., Huang, Q., et al. FakeShield: Explainable image forgery detection and localization via multi-modal large language models. In *Proceedings of the International Conference on Learning Representations, 2025b*.

Zhang, K., Kong, C., Liu, H., Ding, B., Jiang, X., et al. Propose and Rectify: A forensics-driven mllm framework for image manipulation localization. *arXiv preprint, abs/2508.17976*, 2025a.

Zhang, X., Gao, Z., Zhang, B., Li, P., Zhang, X., et al. Adaptive chain-of-focus reasoning via dynamic visual search and zooming for efficient vlms. *arXiv preprint, abs/2505.15436*, 2025b.

Zheng, Z., Yang, M., Hong, J., Zhao, C., Xu, G., et al. DeepEyes: Incentivizing “thinking with images” via reinforcement learning. *arXiv preprint, abs/2505.14362*, 2025.

Zhou, P., Han, X., Morariu, V. I., and Davis, L. S. Learning rich features for image manipulation detection. In *Proceedings of the IEEE/CVF Conference on Computer Vision and Pattern Recognition*, pp. 1053–1061, 2018.

A. Overview

In this appendix, we provide a comprehensive supplement to the main paper, detailing the dataset composition, the rationale behind forensic tools and reasoning trajectory construction, implementation protocols, and extended experimental analysis of ForgeryVCR. The content is organized as follows:

- **Section B (Dataset Composition and Scale)** details the specific composition of training and evaluation datasets used in ForgeryVCR. Furthermore, we provide a comparative analysis of training data magnitude, demonstrating our method’s superior data efficiency against existing state-of-the-art approaches.
- **Section C (Hybrid Forensics Toolbox Construction)** presents a rigorous analysis of the forensic tool selection process. This includes both quantitative validation and qualitative rationale for pruning the candidate pool to the selected set (ELA, FFT, NPP), highlighting their mutual orthogonality and effectiveness.
- **Section D (Visual-Centric Trajectory Synthesis Details)** elaborates on the data generation algorithms described in the main text, specifically the Gain-Driven Tool Selection and Multi-Trajectories Synthesis modules. We also provide statistical breakdowns of the synthesized reasoning paths.
- **Section E (Training Implementation and Reward Formulation)** provides the precise mathematical definitions of the reward components utilized in the RL stage. Additionally, we list the exact training hyperparameters and model configurations for the main results, ablation studies, and the preliminary Lightweight Tool-Specific Fine-Tuning.
- **Section F (Extended Experimental Analysis)** presents supplementary experimental results to substantiate the model’s robustness. This includes bounding-box level localization metrics (BBox-IoU), sensitivity analysis of RL reward weights, and performance curves under various image degradations.
- **Section G (Qualitative Visualization and Analysis)** offers visual insights into the model’s decision-making process. This covers the evolution of tool usage policies after RL optimization, a visual comparison between Visual-Centric and Visual-Textual reasoning paradigms, and qualitative examples of predicted masks against baseline methods.
- **Section H (Prompt Templates)** lists the exact system prompts and template structures used for constructing the Visual-Centric Chain-of-Thought data, ensuring the reproducibility of our data generation pipeline.

B. Dataset Composition and Scale

B.1. Dataset Composition

To ensure reproducibility, we detail the specific data distribution utilized for model training and evaluation (see Table 8).

Training Data. The Strategic Tool Learning Pipeline involves two phases: Supervised Fine-Tuning (SFT) and Reinforcement Learning (RL).

- **SFT** We strictly utilize a balanced subset of the CASIA v2 dataset (Dong et al., 2013), consisting of 5,123 authentic and 5,123 tampered images. This equilibrium prevents the model from developing a bias toward authenticity during initialization.
- **RL** To enhance policy robustness, we expand the training distribution by incorporating the IMD2020 dataset (Novozamsky et al., 2020) and a subset of the FantasticReality dataset (Kniaz et al., 2019). For FantasticReality, we sample a balanced set of 5,000 authentic and 5,000 tampered images to maintain training efficiency.

Evaluation Data. We employ a comprehensive suite of eight benchmarks to assess generalization across Splicing (SP), Copy-Move (CM), and Removal/Inpainting (INP). These include CASIA v1 (Dong et al., 2013), Coverage (Wen et al., 2016), CocoGlide (Guillaro et al., 2023), NIST16 (Guan et al., 2019), Korus (Korus & Huang, 2017), DSO-1 (De Carvalho et al., 2013), Columbia (Hsu & Chang, 2006), and In-the-wild (Huh et al., 2018). Notably, the In-the-wild dataset consists exclusively of manipulated images, providing a rigorous test for false negative rates.

B.2. Training Data Scale Comparison

To demonstrate the data efficiency of ForgeryVCR, we compare our training data magnitude with existing state-of-the-art methods in Table 9. Current IFDL approaches often rely on massive-scale datasets to enforce generalization. Specialist networks like TruFor and SAFIRE utilize extensive repositories exceeding 900,000 images, combining public benchmarks with large-scale self-synthesized data. Similarly, recent MLLM-based adaptations such as SIDA and FakeShield require substantial data volumes (over 100,000 images).

In contrast, ForgeryVCR achieves SOTA performance with a substantially more compact data footprint of approximately **22,670 images**. By strategically curating high-quality samples for visual-centric reasoning, our framework effectively maximizes the diagnostic value of each sample, demonstrating that robust forgery detection can be achieved without large scale training.

Table 8. Detailed statistics of the training and test datasets utilized in ForgeryVCR. To provide a granular view of the training pipeline, we explicitly categorize the training data into the Cold-Start phase and the RL phase. The table lists the number of Real and Forged images, along with the specific manipulation types covered: Splicing (SP), Copy-Move (CM), and Inpainting/Removal (INP).

Split	Stage	Dataset	Number of Images		Forgery Types		
			Real	Forged	SP	CM	INP
Train	SFT	CASIA v2	5,123	5,123	✓	✓	
	RL	IMD2020	414	2,000	✓	✓	✓
		FantasticReality	5,000	5,000	✓		✓
Test	-	CASIA v1	800	920	✓	✓	
		Coverage	100	100		✓	
		CocoGlide	512	512			✓
		NIST16	876	564	✓	✓	✓
		Korus	220	220	✓	✓	
		DSO-1	100	100	✓		
		Columbia	183	180	✓		
		In-the-wild	0	201	✓		

Table 9. Comparison of training dataset composition and total data volume across different state-of-the-art methods. The term “Self-synthesized dataset” refers to data generated by the authors using custom pipelines (e.g., COCO-based synthesis). Our method, ForgeryVCR, is highlighted to demonstrate its data efficiency.

Method	Training Datasets	Volume
MVSS-Net	CASIA v2	12,554
IF-OSN	WEI	11,284
TruFor	CASIA v2, IMD20, FantasticReality, tampCOCO, Flickr, DPReview, Self-synthesized dataset	900,254
CoDE	CASIA v2, IMD20, tampCOCO	11,133
HDF-Net	CASIA v2, Self-synthesized dataset	32,663
PIM	CASIA v2	12,614
SAFIRE	CASIA v2, IMD20, FantasticReality, tampCOCO	900,254
FakeShield	CASIA v2, FantasticReality, FFHQ, FaceAPP, COCO, AIGC-Editing	105,937
SIDA	SID-Set	210,000
ForgeryVCR	CASIA v2, IMD20, FantasticReality	22,670

C. Hybrid Forensics Toolbox Construction

In this section, we provide a detailed analysis of the forensic tool selection process. We visualize the outputs of the full candidate pool and articulate the rationale for excluding specific descriptors based on redundancy, visual distinctiveness, and their compatibility with the visual encoders of MLLMs.

C.1. Initial Candidate Pool

Our initial investigation explored a diverse set of **8 forensic descriptors** spanning spatial, frequency, and generative domains. As illustrated in Fig. 7, we visualize the outputs of these tools alongside the ground truth (GT). The candidates include:

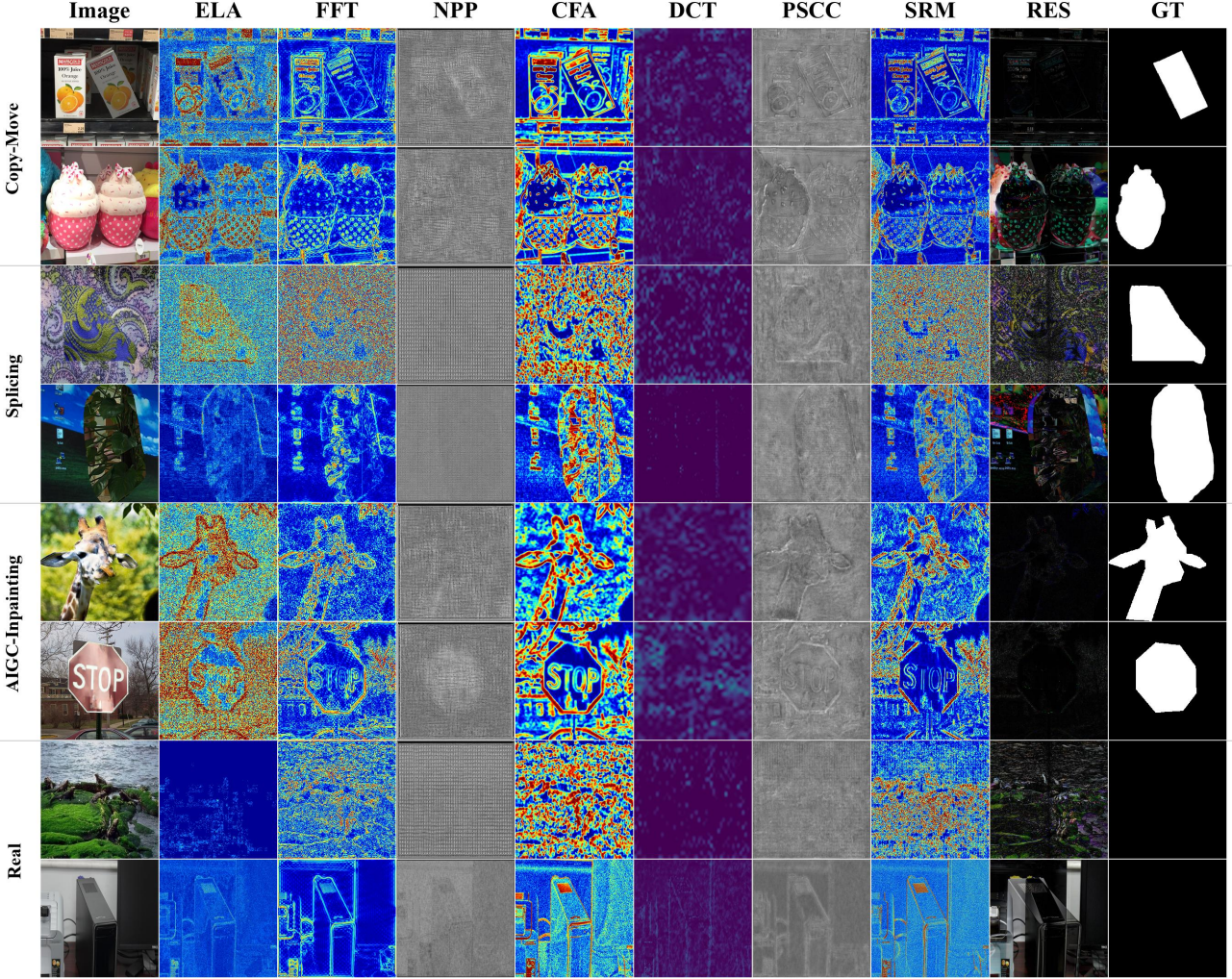


Figure 7. Visual comparison of the initial candidate pool of forensic tools across splicing, copy-move, removal and Inpainting manipulations. Our final selection (ELA, FFT, NPP) retains the most visually distinct features, whereas others exhibit redundancy or lack perceptible visual cues for the MLLM.

- **Spatial & Statistical Consistency Tools:**

- **Error Level Analysis (ELA)** (Lu et al., 2025) (Selected): This method highlights discrepancies in compression artifacts. By computing the difference between the original image and a re-compressed version (typically at fixed JPEG quality), ELA reveals regions that have undergone different compression histories compared to the background.
- **Noise Print++ (NPP)** (Guillaro et al., 2023) (Selected): A learned noise extractor that captures camera model

fingerprints (PRNU) and anomalous noise residuals. It excels at exposing inconsistencies where the local sensor noise pattern deviates from the global camera signature, often creating a sharp contrast in manipulated areas.

- **Progressive Spatio-Channel Correlation (PSCC)** (Liu et al., 2022) (Excluded): Derived from the PSCC-Net architecture, this tool utilizes a Spatio-Channel Correlation Module to capture dense feature correlations. It produces a probability map intended to highlight manipulation masks by analyzing both spatial and channel-wise inconsistencies in a coarse-to-fine manner.
- **Spatial Rich Models (SRM)** (Su et al., 2024) (Excluded): Originally designed for steganalysis, these are a set of high-pass filters that extract local pixel dependencies. SRM visualizes high-frequency residuals to expose disruptions in local texture statistics that are invisible to the naked eye.
- **Color Filter Array (CFA)** (Zhou et al., 2018) (Excluded): This tool visualizes statistical traces of the demosaicing process. Since most cameras use a Bayer filter, image manipulation often disrupts the periodic interpolation patterns. The tool aims to expose these disruptions as visual artifacts in the probability map.

- **Frequency Domain Tools:**

- **Fast Fourier Transform (FFT)** (Kashiani et al., 2025) (Selected): Transforms the spatial image signal into the frequency spectrum. It is particularly effective at revealing periodic anomalies, such as grid-like artifacts left by GAN upsampling or checkerboard patterns from resizing, which appear as distinct high-frequency spectral peaks.
- **Discrete Cosine Transform (DCT)** (Kwon et al., 2022) (Excluded): Analyzes frequency coefficients within local blocks (e.g., 8×8). It is widely used to detect double JPEG compression by analyzing the histogram of coefficients, visualizing block-level inconsistencies in the frequency domain.

- **Generative Domain Tools:**

- **VAE Reconstruction Residuals (RES)** (Excluded): Inspired by the concept of reconstruction-based detection (Wang et al., 2023), we utilize the **KL-regularized Autoencoder (VAE)** from **Stable Diffusion v2.1-base** to compute pixel-wise residuals. Specifically, we encode the image into the latent space and decode it back to the pixel space. The resulting map visualizes the absolute difference between the original input and the VAE reconstruction. The hypothesis is that the VAE, pre-trained on large-scale authentic images, yields higher reconstruction errors in regions containing unnatural manipulation artifacts or high-frequency anomalies that fall outside its learned latent distribution.

C.2. Qualitative Analysis and Tool Selection Rationale

As observed in Fig. 7, simply stacking all forensic visualizations introduces significant noise and redundancy. Based on the visual evidence from the initial candidate pool, we derived the following rationale for our pruning process, ensuring the selected tools provide the distinctest visual signals for the MLLM.

Redundancy in Spatial Residuals (CFA & SRM). While CFA and SRM are staples in traditional steganalysis, their visual outputs in Fig. 7 appear as high-frequency visual static (random noise). For instance, in the first row (spliced box), although CFA captures some traces, the signal is buried within the background noise. This noisy texture is semantically similar to natural high-frequency details (like gravel or foliage), making it difficult for general-purpose vision encoders (e.g., CLIP, SigLIP) to distinguish forgery from texture. In contrast, the selected **FFT** transforms these invisible periodicities into distinct, star-like geometric patterns (Row 2), and **NPP** highlights the manipulated region with significantly higher contrast and cleaner background suppression. We exclude CFA and SRM to avoid flooding the model with ambiguous noise patterns.

Functional Overlap in Consistency Checks (PSCC vs. NPP). Both tools aim to identify inconsistencies in source fingerprints or lighting. However, a visual comparison in Fig. 7 reveals a stark difference in clarity. **PSCC** (Column 6) tends to produce muddy or diffuse gray-scale heatmaps where the manipulated region blends into the background with soft edges. Conversely, **NPP** (Column 4) produces a sharp, almost binary-like mask where the tampered region (e.g., the white silhouette in Row 4) stands out vividly against a suppressed gray background. This high Signal-to-Noise Ratio in NPP allows the MLLM to perform precise localization without the ambiguity found in PSCC’s outputs. Thus, we retain NPP as the superior consistency checker.

Visual Ineffectiveness (DCT and RES). Despite their theoretical soundness, these tools fail to produce human- or model-perceptible visual cues in many scenarios.

- **DCT:** As shown in the DCT column of Fig. 7, the resulting maps are predominantly black or dark purple, dominated by grid artifacts. The crucial coefficients that indicate forgery are mathematically present but visually imperceptible to a frozen vision encoder. The lack of salient visual features makes DCT an inefficient token consumer for Visual-CoT.
- **RES (Generative Residuals):** The RES maps rely on reconstruction errors from a VAE. While effective for diffusion-generated artifacts, they suffer from severe texture leak in traditional manipulations. As seen in Row 3 (the group of girls), RES highlights the complex textures of the hair and faces of authentic people just as strongly as potential forgeries. This creates visual confusion, leading the MLLM to hallucinate forgeries on legitimate complex textures.

Consequently, our final **Hybrid Forensics Toolbox** retains only ELA, NPP, FFT, and the Zoom-In mechanism. This configuration maximizes forensic coverage—capturing compression, sensor noise, and frequency anomalies—while ensuring every input visual token carries a distinct, high-contrast forensic signal.

C.3. Quantitative Ablation Study

To determine the effective configuration for the Hybrid Forensics Toolbox, we conducted a rigorous two-step quantitative analysis on the CASIA v2 dataset and generalization benchmarks. This process avoids arbitrary selection by evaluating both the individual capability of each tool and the potential gain from their combination.

Step 1: Individual Tool Effectiveness. First, we assessed the intrinsic value of each forensic descriptor. Following the Lightweight Tool-Specific Fine-tuning protocol mentioned in Section 3.3, we trained separate SFT models for each candidate tool. Each model takes the original RGB image and one specific forensic view (e.g., ELA) as input. We then evaluated these specialist models on the test set.

Table 10 presents the performance of each single-tool expert. The results indicate that ELA, FFT, NPP, and the Zoom-In mechanism individually provide the strongest forensic signals, whereas tools like DCT and RES yield lower performance, suggesting they offer less perceptible information to the MLLM.

Table 10. Performance of single-tool specialist models. Each row represents an MLLM fine-tuned exclusively with the original image and the specified tool. **Zoom-In**, **NPP**, **ELA** and **FFT** demonstrate the most significant individual contributions.

Forensic Tool	Image-level Detection		Pixel-level Localization	
	F1	ACC	F1	IoU
Baseline (RGB Only)	0.5672	0.5926	0.2746	0.2465
+ ELA	0.6973	<u>0.6420</u>	0.4167	0.3731
+ FFT	0.6002	0.6146	0.3276	0.2890
+ NPP	0.5819	0.5956	0.3082	0.2775
+ CFA	0.5959	0.5906	0.3294	0.2968
+ DCT	0.5240	0.5715	0.2590	0.2355
+ PSCC	0.5025	0.5701	0.2542	0.2311
+ RES	0.5105	0.5698	0.2538	0.2300
+ SRM	0.5902	0.6015	0.3304	0.2983
+ Zoom-In	<u>0.6045</u>	0.6615	<u>0.3569</u>	<u>0.3261</u>

Step 2: Theoretical Optimal Performance Analysis. Merely stacking tools can introduce redundancy. To identify the point of diminishing returns, we calculated the *Theoretical Optimal Performance* (Upper Bound) for cumulative tool combinations.

Calculation Method: For a given set of available tools T_{set} , and a specific test sample x , we simulate a Perfect Selector. We aggregate the predictions from all single-tool models trained in Step 1 corresponding to tools in T_{set} . The sample is considered correctly detected/localized if *at least one* tool in T_{set} produces a correct classification or a high-quality mask. Specifically, the theoretical IoU for sample x is defined as $IoU_{best} = \max_{t \in T_{set}} (IoU_t)$.

Table 11 shows the trajectory of this theoretical upper bound as we incrementally add tools. We observe that combining **ELA**, **FFT**, **NPP**, and **Zoom-In** yields a significant performance leap. However, adding subsequent tools (CFA, DCT, etc.) results in marginal gains or saturation. This confirms that the selected subset covers the necessary forensic modalities (compression, frequency, noise, and detail) effectively, while further additions offer redundant information.

Table 11. Theoretical Optimal Performance analysis with cumulative tool integration. The metrics represent the upper bound achievable if the model perfectly selects the best tool from the available subset for each sample. The performance gain saturates after the inclusion of the first four tools.

Tool Configuration									Image-level Detection		Pixel-level Localization	
ELA	FFT	NPP	Zoom	CFA	DCT	PSCC	RES	SRM	F1	ACC	F1	IoU
✓									0.5672	0.5926	0.2746	0.2465
✓	✓								0.6920 (+12.5%)	0.6420 (+4.9%)	0.4167 (+14.2%)	0.3731 (+12.7%)
✓	✓	✓							0.7678 (+7.6%)	0.7479 (+10.6%)	0.4538 (+3.7%)	0.4064 (+3.3%)
✓	✓	✓	✓						0.8009 (+3.3%)	0.7869 (+3.9%)	0.4801 (+2.6%)	0.4296 (+2.3%)
✓	✓	✓	✓	✓					0.8773 (+7.6%)	0.8776 (+9.1%)	0.4972 (+1.7%)	0.4450 (+1.5%)
✓	✓	✓	✓	✓	✓				0.8805 (+0.3%)	0.8807 (+0.3%)	0.4981 (+0.1%)	0.4457 (+0.1%)
✓	✓	✓	✓	✓	✓	✓			0.8812 (+0.1%)	0.8823 (+0.2%)	0.4985 (+0.0%)	0.4462 (+0.1%)
✓	✓	✓	✓	✓	✓	✓	✓		0.8812 (+0.0%)	0.8823 (+0.0%)	0.4992 (+0.1%)	0.4466 (+0.0%)
✓	✓	✓	✓	✓	✓	✓	✓	✓	0.8812 (+0.0%)	0.8823 (+0.0%)	0.4996 (+0.0%)	0.4469 (+0.0%)
✓	✓	✓	✓	✓	✓	✓	✓	✓	0.8817 (+0.1%)	0.8839 (+0.2%)	0.5003 (+0.1%)	0.4475 (+0.1%)

Table 12. Detailed ablation study on specific combinations within the selected toolset. We evaluate permutations of ELA, FFT, and NPP, both with and without the Zoom-In mechanism. The study encompasses 15 distinct configurations, ranging from single-tool baselines to the comprehensive **Full Suite** (highlighted in blue), which yields the best performance.

Toolbox Components				Image-level Detection		Pixel-level Localization	
ELA	FFT	NPP	Zoom-In	F1	ACC	F1	IoU
✓			✓	0.6617	0.6786	0.4404	0.3994
	✓		✓	0.6814	0.6958	0.4714	0.4281
		✓	✓	0.6643	0.6764	0.4482	0.4076
✓	✓		✓	0.6648	0.6788	0.4428	0.4031
✓		✓	✓	0.6526	0.6811	0.4433	0.4051
	✓	✓	✓	0.6860	0.6822	0.4618	0.4192
✓	✓	✓	✓	0.7242	0.6893	0.5215	0.4699
	✓			0.6742	0.6881	0.4235	0.3844
		✓		0.6588	0.6830	0.3951	0.3596
			✓	0.6543	0.6756	0.4027	0.3656
✓	✓			0.6188	0.6578	0.3735	0.3383
✓		✓		0.6322	0.6584	0.3951	0.3597
	✓	✓		0.5896	0.6523	0.3512	0.3201
✓	✓	✓		0.6903	0.6875	0.4464	0.4049

Having established that ELA, FFT, NPP, and Zoom-In constitute the theoretically optimal subset above, we now proceed to empirically validate their synergy. We conduct a fine-grained SFT ablation study to confirm that these components offer complementary forensic information and that the full suite outperforms any partial combination.

Ablation on Selected Tool Combinations. To validate the internal synergy of the proposed toolbox, we perform a detailed breakdown of the components. While Table 7 in the main text establishes the superiority of the full framework, this granular analysis isolates the contribution of each forensic descriptor (ELA, FFT, NPP) and their interaction with the Zoom-In mechanism.

Table 12 presents the SFT performance across different subsets, revealing the intrinsic synergy within our toolbox. The results demonstrate a strong complementarity among forensic tools, where the combination of ELA, FFT, and NPP consistently outperforms single-tool baselines by covering diverse manipulation traces—ranging from compression artifacts and frequency anomalies to sensor noise. Crucially, this forensic foundation is further amplified by the Zoom-In mechanism, which universally lifts performance across all metrics. This confirms that visual refinement acts as a powerful attention guide, enabling the MLLM to apply global forensic insights to precise local regions, with the complete suite achieving the best overall performance.

D. Visual-Centric Trajectory Synthesis Details

D.1. Trajectory Synthesis Pipeline

The construction of the Cold-Start SFT dataset involves a rigorous process of model-based filtration and trajectory synthesis. We first establish a foundation by training lightweight specialist models to assess the intrinsic utility of each forensic tool.

Lightweight Tool-Specific Fine-Tuning. To obtain the performance metrics required for our gain-driven tool selection, we train a set of independent specialist models on the Cold-Start training dataset. These models include one **Tool-Free Baseline** and separate **Single-Tool Experts** for each candidate tool (ELA, NPP, FFT, and Zoom-In). The precise data formatting for these models is presented in the following data structure blocks. The Tool-Free Baseline relies solely on the original image, whereas the Single-Tool Experts incorporate specific forensic visualizations alongside expert-guided prompts to facilitate visual diagnostics.

Data Structure 1: Tool-Free Baseline

```
{
  "role": "user",
  "content": "<image>What is the status of this image, real or fake? If you detect manipulation, please provide the bounding boxes."
},
{
  "role": "assistant",
  "content": "<answer>real</answer>"
}
```

Data Structure 2: Single-Tool Expert (e.g., FFT)

```
{
  "role": "user",
  "content": "<image><image>The first image is the original input, and the second is its FFT High-Frequency heatmap. In the heatmap, red or bright areas represent strong high-frequency energy... [Tool Analysis Instructions]... If the image is authentic, output <answer>real</answer>. If manipulated, detect and output fake and the bounding box..."
},
{
  "role": "assistant",
  "content": "<answer>fake, <|box_start|>x_min,y_min,x_max,y_max<|box_end|></answer>"
}
```

The detailed hyperparameters for this lightweight fine-tuning stage are provided in Table 14. Notably, we employ a short training schedule (5 epochs) and strictly visual-input-only prompting to evaluate the raw perceptibility of the forensic features without the aid of linguistic and visual-centric reasoning chains.

Algorithm. To ensure the instruction-tuning dataset fosters genuine visual-centric reasoning rather than hallucination or tool redundancy, we formalize the data construction process into two cooperative phases as detailed in Algorithm 1. The primary objective is to curate a set of reasoning trajectories that are both diagnostically valid and diverse in complexity. In the first phase, denoted as Gain-Driven Tool Selection, we rigorously filter the candidate pool T_{pool} to retain only those forensic operators capable of revealing imperceptible artifacts. By evaluating the performance gain P_t of each tool-specific expert against a tool-free baseline P_{base} and a validity threshold τ , we isolate the discriminative signals essential for the specific sample (x, y) . This process simultaneously executes Intractable Sample Removal to discard instances where all models fail to extract useful features, returning an optimized and ranked tool sequence T_{rank} . Subsequently, the Multi-Trajectories Synthesis phase utilizes this ranked sequence to construct a comprehensive set of reasoning paths P_{aug} . To cultivate an adaptive policy capable of handling varying difficulty levels, we synthesize trajectories ranging from direct visual assessment to independent evidence collection and progressive multi-view verification. This structured diversification ensures the model

encounters specific tool invocations only when they yield tangible information gains, thereby mitigating dependency on ineffective operations.

Regarding the truncation parameter K mentioned in Sec. 3.3, we apply a dynamic setting to balance the SFT training data: $K = 4$ for tampered samples and $K = 2$ for authentic ones. Since the lightweight specialist models inherit the MLLM's intrinsic perception on real images, achieving high accuracy with minimal assistance, restricting K for authentic samples prevents redundant tool invocations while preserving valuable instruction data.

Notation. In Algorithm 1, (x, y) denotes an image-label pair; M_{base} is the tool-free baseline model and $\{M_t\}$ are single-tool expert models; V_t represents the forensic tool map generated by tool t ; the operator \oplus denotes concatenation; $\text{Eval}(\cdot)$ returns the performance metric P ; and \mathcal{S}_{reject} indicates sample rejection via ISR.

Algorithm 1 Data Construction Pipeline: Tool Selection & Trajectory Synthesis

Stage 1: Gain-Driven Tool Selection & Ranking

```

1: Input: Sample  $(x, y)$ , Pool  $T_{pool}$ , Models  $M_{base} \cup \{M_t\}$ , Threshold  $\tau$ 
2: Output: Ranked tool sequence  $T_{rank}$  or Reject Signal  $\mathcal{S}_{reject}$ 
3: Calc baseline  $P_{base} \leftarrow \text{Eval}(M_{base}, x)$ 
4: Calc tool perfs  $P_t \leftarrow \text{Eval}(M_t, x \oplus V_t) \forall t$ 
5:  $P_{max} \leftarrow \max(P_{base}, \max_t P_t)$ 
6: // Execute Intractable Sample Removal
7: if  $P_{max} < \tau$  then
8:   Return  $\mathcal{S}_{reject}$ 
9: end if
10: // Select & Rank Gain-Driven Tools
11: Initialize  $T_{rank} \leftarrow \emptyset$ 
12: for each tool  $t \in T_{pool}$  do
13:   if  $P_t > \max(P_{base}, \tau)$  then
14:      $T_{rank} \leftarrow T_{rank} \cup \{t\}$ 
15:   end if
16: end for
17: Sort  $T_{rank}$  by  $P_t$  in descending order
18: Return  $T_{rank}$ 

```

Stage 2: Multi-Trajectories Synthesis

```

1: Input: Ranked Sequence  $T_{rank}$ , Truncation  $K$ 
2: Output: Reasoning Trajectories  $P_{aug}$ 
3: Init trajectories  $P_{aug} \leftarrow \{\emptyset\}$  // Direct Assessment
4: if  $T_{rank} \neq \emptyset$  then
5:    $T'_{rank} \leftarrow T_{rank}[1 : \min(|T_{rank}|, K)]$  // Top-K Truncation
6:   // Type 1: Independent Evidence Paths
7:   for each tool  $t_i \in T'_{rank}$  do
8:      $P_{aug} \leftarrow P_{aug} \cup \{[t_i]\}$ 
9:   end for
10:  // Type 2: Accumulative Evidence Paths
11:  if  $|T'_{rank}| \geq 2$  then
12:    for  $k = 2$  to  $|T'_{rank}|$  do
13:       $S_{accum} \leftarrow [t_1, \dots, t_k]$  // Sequence up to  $k$ 
14:       $P_{aug} \leftarrow P_{aug} \cup \{S_{accum}\}$ 
15:    end for
16:  end if
17: end if
18: Return  $P_{aug}$ 

```

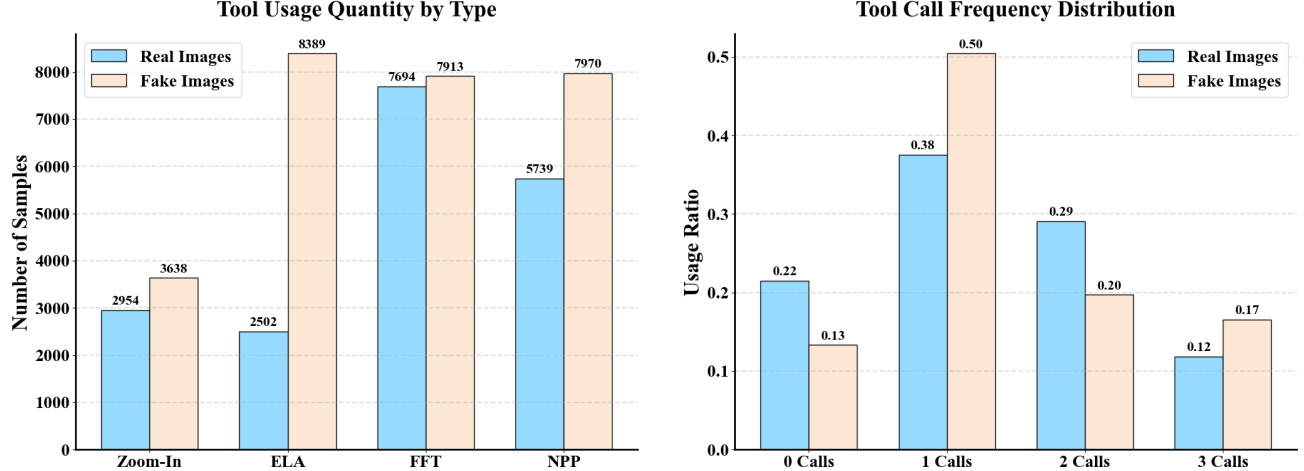
D.2. Statistics of Synthesized Reasoning Trajectories


Figure 8. Statistical analysis of the synthesized SFT trajectories. **Left:** The frequency of specific tool invocations, showing high selectivity for ELA on manipulated samples. **Right:** The distribution of reasoning chain lengths, indicating that manipulated images generally require deeper multi-tool verification compared to authentic ones.

To contextualize the statistics presented here, we refer to the Trajectory Synthesis Pipeline detailed in Appendix D.1. The

Table 13. Statistics of the SFT dataset after applying the visual-centric trajectories synthesis pipeline. **Unique Source Images** refers to the distinct samples retained after Intractable Sample Removal (ISR). **Reasoning Trajectories** denotes the total number of logical chains generated via Multi-Trajectories Synthesis (MTS), effectively expanding the training data.

Category	Authentic	Tampered
Unique Source Images (Post-ISR)	4,961	3,987
Reasoning Trajectories (Post-MTS)	16,645	17,408

initial specialist models were evaluated on the CASIA v2 training set to derive the Gain-Driven Tool Selection policy. This ensures that the constructed reasoning paths are derived from a controlled distribution where the efficient tool usage is empirically verified.

Dataset Filtering and Expansion. Table 13 quantifies the dual effect of our pipeline. First, the Intractable Sample Removal (ISR) acts as a quality filter, discarding approximately 22% of manipulated images where forensic tools failed to yield perceptible evidence. This step is critical to prevent the model from hallucinating explanations for undetectable forgeries. Second, the Multi-Trajectories Synthesis (MTS) expands these filtered images into a total of 34,053 diverse reasoning trajectories. This one-to-many mapping enables the model to learn adaptive investigation strategies—ranging from direct visual assessment to complex multi-tool verification—rather than memorizing a single fixed path for each image.

Tool Usage Patterns. Fig. 8 illustrates the distribution of tool invocations within these trajectories, highlighting two key behaviors:

- **Tool Selectivity:** As shown in the left panel, *Error Level Analysis (ELA)* is invoked significantly more often for forged images (8,389) than for authentic ones (2,502). This confirms that ELA serves as a specific indicator for compression anomalies, whereas FFT and NPP act as broader validity checks applicable to both classes.
- **Reasoning Depth:** The right panel reveals that authentic images frequently trigger shorter reasoning chains (0 or 1 tool calls), suggesting that visual integrity is often established quickly. In contrast, manipulated images shift towards longer chains (1 to 3 calls), validating that our pipeline successfully synthesizes complexity-aware reasoning paths that deepen investigation when anomalies are suspected.

D.3. Data Formulation Details

In this section, we elaborate on the construction of the ground-truth annotations used for training. To derive the ground truth bounding boxes utilized in the objects field, we calculate the minimum bounding rectangle for each connected component within the pixel-level manipulation mask provided in the CASIA v2 and other forensic datasets. To ensure the annotations represent meaningful forensic targets rather than annotation noise, we apply a filtration strategy that discards connected components smaller than 100 pixels or constituting less than 0.05% of the total image area. This rigorous filtering ensures that the supervision signal during the Supervised Fine-Tuning and Reinforcement Learning stages directs the model toward salient manipulation regions.

To intuitively elucidate the distinction between the conventional Visual-Textual CoT and our proposed Visual-Centric CoT, we present comparative visualization cases representing the input-output structures of both paradigms. Unlike the Visual-Textual CoT, which relies heavily on linguistic descriptions of high-level semantics, the Visual-Centric CoT explicitly incorporates tool execution codes and visual intermediates into the reasoning chain. These visualizations demonstrate how our framework grounds the verification process in tangible forensic evidence rather than ambiguous textual rationale, effectively mitigating semantic hallucinations. The exact system and user prompt templates governing these interactions are provided in Appendix H.1.

D.4. Construction of Visual-Textual CoT Data

To construct the *Visual-Textual CoT* variant utilized in our ablation studies, we extend the reasoning trajectories P_{aug} generated via the Multi-Trajectories Synthesis (Algorithm 1). It is important to note that the sequence of tool invocations and the final decision path remain identical to the *Visual-Only* version; the only difference lies in the insertion of linguistic rationales (wrapped in `<think>` tags) that explain the visual evidence.

To generate these high-fidelity textual rationales, we explicitly employ **Qwen-2.5-VL-72B-Instruct** (Bai et al., 2025) as the

Teacher MLLM. It is crucial to distinguish this data generator from our target student model, **Qwen-3-VL-4B-Instruct**, utilized during the training phase. We select the 72B variant specifically for its superior visual reasoning capabilities and vast parameter scale, which enable it to synthesize intricate forensic descriptions that the smaller 4B model can subsequently learn to mimic through knowledge distillation.

To provide a precise visual reference and ensure reproducibility during the teacher's generation process, we strictly follow a standardized **Mask-Overlay Prompting Strategy**. Specifically, the binary ground-truth mask is first thresholded to isolate the manipulated region. We then apply an alpha-blending process where the manipulated region is rendered in a salient red color (RGB: 255, 0, 0) and superimposed onto the original image with a fixed transparency coefficient of $\alpha = 0.5$. This configuration ensures that the specific location of the forgery is explicitly highlighted to guide the model's attention, while the semi-transparent nature of the overlay preserves the underlying textural details necessary for analyzing visual artifacts.

Addressing the concern regarding the teacher model's potential dependency on the explicit mask, we provide the following clarification:

Concern: Does providing the ground-truth mask cause the teacher model to rely on the overlay rather than simulating genuine forensic findings?

Response: We address this trade-off by drawing upon established methodologies in Visual Chain-of-Thought (V-CoT) literature (Su et al., 2025; Wang et al., 2025). Existing approaches for synthesizing reasoning trajectories typically fall into two categories:

- **Autonomous Exploration via Strong Teachers (Su et al., 2025):** This paradigm leverages the superior visual perception of large-scale models (e.g., GPT-4o) to autonomously plan action trajectories based on few-shot prompts. The teacher model functions as an autonomous planner, determining tool selection and execution sequences. While flexible, this approach relies heavily on the teacher's intrinsic ability to detect the initial anomaly without assistance. It typically requires a post-hoc filtering stage to discard invalid or hallucinatory paths.
- **Fixed-Trajectory Supervision for Specialized Tasks (Wang et al., 2025):** This approach is preferred when the investigation logic is finite and well-defined. Instead of letting the model wander, it employs pre-designed prompt templates (e.g., “Global Analysis → Tool Usage → Local Verification”) to force the teacher model into specific, high-gain reasoning patterns. By acting as a “director,” the framework ensures the generated data covers diverse and effective error-correction or refinement scenarios that a model might not spontaneously attempt.

Justification for Our Approach: We align with the **Fixed-Trajectory** paradigm for a critical reason: unlike general visual tasks, forensic artifacts (e.g., weak PRNU traces or subtle compression inconsistencies) are often imperceptible to even the strongest commercial MLLMs without tool assistance. An autonomous exploration approach would likely fail at the first step, as the teacher would not perceive the “suspicious region” required to trigger the correct tool. Therefore, we utilize the **Ground-Truth Mask** as a necessary “director’s cue.” It does not serve as the final answer but rather anchors the teacher’s attention, enabling it to simulate a successful detection and localization trajectory (e.g., describing the noise mismatch at that specific location) that would otherwise be impossible to synthesize.

Aligning with the **Fixed-Trajectory** paradigm, we implement the Mask-Overlay strategy. Our rationale and specific mitigation measures are as follows:

1. **Necessity of Fixed Trajectories in Forensics:** Unlike general visual tasks where objects are salient, forensic artifacts (e.g., noise inconsistencies in ELA) are visually subtle and often imperceptible without precise localization. Relying solely on the teacher model’s autonomous exploration poses a high risk of hallucination or missed detection, which would degrade the quality of the training data. Therefore, we adopt the fixed-trajectory strategy to ensure the teacher attends to the exact tampered region.
2. **Mitigation via System Prompting:** To prevent the model from simply describing the “red mask,” we enforce a strict negative constraint in the system prompt: *“You must treat the red overlay solely as a location hint. Do NOT mention the red color or the mask itself. Focus your description entirely on the visual anomalies (texture, noise, resolution) visible BENEATH the overlay.”* This ensures that while the mask guides *where* to look, the generated rationale describes *what* forensic features are present.

Based on the structure of the trajectory derived in Stage 2 (Algorithm 1), we categorize the generation process into three distinct prompt templates. The No-Tool Direct Assessment is applied when no external tools are retrieved. In cases where a single expert tool is selected, the Single-Tool Analysis is utilized. Finally, the Multi-Tool Synthesis is employed when multiple tools are involved.

- **No-Tool Direct Assessment:** Applied when $P_{aug} = \{\emptyset\}$. The model is prompted to identify global semantic inconsistencies or obvious visual artifacts without external aids.
- **Single-Tool Analysis:** Applied when $P_{aug} = \{[t_i]\}$. The prompt focuses on interpreting the specific feature map (e.g., ELA noise patterns) returned by the selected expert tool $t_i \in T_{rank}$.
- **Multi-Tool Synthesis:** Applied when $P_{aug} = \{[t_1, \dots, t_k]\}$. The model is tasked with synthesizing evidence from multiple views to form a comprehensive verdict.

The specific prompt templates corresponding to these three categories are detailed in [Appendix H.2](#).

E. Training Implementation and Reward Formulation

E.1. Detailed Reward Formulation

In this section, we provide the precise mathematical definitions and implementation details for the reward components utilized in the Reinforcement Learning stage.

Variable Definitions and Parsing Logic. Let $\mathcal{B}_{gt} = \{b_1, \dots, b_M\}$ denote the set of ground-truth bounding boxes for a manipulated image, where $M \geq 1$. Similarly, let $\hat{\mathcal{B}} = \{\hat{b}_1, \dots, \hat{b}_N\}$ represent the set of predicted bounding boxes. To compute the rewards, we first parse the model’s raw textual completion to extract the predicted label \hat{c} , the bounding boxes $\hat{\mathcal{B}}$, and the tool usage history u_t .

- **Label and BBox Extraction:** We extract the content within the `<answer>...</answer>` tags. The label \hat{c} is determined by keyword matching (e.g., “fake” or “real”). If $\hat{c} = \text{fake}$, we identify the localization outputs encapsulated by the special tokens `<|box_start|>` and `<|box_end|>`. We then parse the coordinate strings within these tokens (formatted as $(x_1, y_1), (x_2, y_2)$) using regular expressions to construct the set $\hat{\mathcal{B}}$. If no valid coordinates are found, $\hat{\mathcal{B}}$ is treated as an empty set \emptyset .
- **Tool Usage Detection:** We define $u_t \in \{0, 1\}$ by scanning the conversation history. $u_t = 1$ if we detect a valid `<tool_call>` tag containing a supported function name (ELA, FFT, NPP, or Zoom-In) or a `<tool_response>` indicating prior execution; otherwise, $u_t = 0$.

Classification Reward (R_{cls}). This component ensures the model correctly distinguishes between authentic and manipulated images. Crucially, to mitigate semantic hallucinations where the model predicts “fake” without locating any actual tampering traces, we impose a validity constraint derived from the parsing logic: for manipulated samples, the reward is granted only if the prediction is accompanied by at least one valid bounding box.

$$R_{cls} = \mathbb{I}(\hat{c} = c) \cdot \begin{cases} 1, & \text{if } c = \text{real} \\ \mathbb{I}(\hat{\mathcal{B}} \neq \emptyset), & \text{if } c = \text{fake} \end{cases} \quad (6)$$

Localization Reward (R_{loc}). To foster precise spatial reasoning, this reward evaluates the Intersection over Union (IoU) between the predicted regions and the ground truth. Since both the prediction and ground truth may contain multiple disjoint bounding boxes (i.e., $|\hat{\mathcal{B}}| \geq 1$ and $|\mathcal{B}_{gt}| \geq 1$), a simple one-to-one IoU is insufficient. We employ the **Hungarian matching algorithm** (also known as the Kuhn-Munkres algorithm) to solve this assignment problem:

1. We construct a cost matrix C of size $N \times M$, where each element $C_{ij} = 1 - \text{IoU}(\hat{b}_i, b_j)$.
2. We apply the Hungarian algorithm to find the optimal assignment of predicted boxes to ground-truth boxes that minimizes the total cost (maximizes total IoU).

3. The final metric, denoted as HungarianIoU($\hat{\mathcal{B}}, \mathcal{B}_{gt}$), is calculated as the mean IoU of these matched pairs.

This reward is applied exclusively to manipulated samples to prevent optimization conflicts on authentic images (where $\mathcal{B}_{gt} = \emptyset$).

$$R_{loc} = \text{HungarianIoU}(\hat{\mathcal{B}}, \mathcal{B}_{gt}) \cdot \mathbb{I}(c = \text{fake}) \quad (7)$$

Tool Utility Reward (R_{tool}). This conditional reward is designed to cultivate an efficient investigation policy, penalizing the MLLM for invoking forensic tools when they are unnecessary (e.g., on obvious real images) or ineffective (yielding no informational gain). Based on the parsed tool usage u_t , a reward is deemed valid only if the tool invocation leads to a correct final verdict. For manipulated images, we impose a stricter requirement: the tool must contribute to a high-precision localization, defined by the Hungarian IoU exceeding a threshold τ_{IoU} (set to 0.5).

$$R_{tool} = u_t (\mathbb{I}_{c=\text{real}} R_{cls} + \mathbb{I}_{c=\text{fake}} \mathbb{I}_{\text{HungarianIoU} > \tau_{IoU}}) \quad (8)$$

E.2. Implementation Details

To ensure the reproducibility of our results and provide a comprehensive understanding of the experimental variables, we detail the specific configurations used for the main benchmarks and the comparative ablation studies.

Main Results Configuration. To substantiate the state-of-the-art performance reported in Table 1 and Table 2, we rigorously evaluated different reasoning paradigms. As discussed in Section 4, our preliminary investigation compared the efficacy of Visual-Textual CoT against the proposed Visual-Centric (Visual-Only) CoT. Empirical evidence demonstrated that the inclusion of intermediate linguistic rationales often introduced semantic hallucinations, whereas the Visual-Centric approach yielded superior robustness; thus, the latter was adopted as the standard configuration for all main results. Regarding the post-processing refinement, the segmentation masks are generated by the Hiera-Large variant of the Segment Anything Model 2 (SAM 2 Hiera Large), which receives the bounding box predicted by our model as a visual prompt. It is imperative to clarify that while SAM 2 serves as a refinement module for pixel-level segmentation, the fundamental region-level localization capability is acquired through our strategic tool learning pipeline. The ForgeryVCR explicitly identifies the manipulated regions and generates the bounding box coordinates that guide the segmentation process. For an assessment of the model’s intrinsic region-level localization performance without the assistance of the segmentation head, we refer readers to the Bounding Box IoU (BBox-IoU) analysis provided in Appendix F.4.

Table 14. Comprehensive overview of training configurations across all experiments. The table details the specific settings for the reasoning paradigms (CoT), SFT data strategies (ISR: Intractable Sample Removal, MTS: Multi-Trajectories Synthesis), RL reward components (R_{cls} , R_{loc} , R_{tool}), training duration, and trainable modules. “General MLLMs” refers to the baselines listed in Table 3.

Experiment / Method	Backbone	CoT Modality		SFT Strategy		RL Rewards			Duration (Steps)	Trainable Modules		
		Visual	Textual	ISR	MTS	R_{cls}	R_{loc}	R_{tool}		Aligner	Vision	LLM
Base Model (Zero-shot)	Qwen3-VL-4B	×	×	×	×	×	×	×	-	-	-	-
Lightweight Tool-Specific FT	Qwen3-VL-4B	×	×	×	×	×	×	×	5 Epochs	✓	✓	✗
Fine-tuning General MLLMs	Various	×	×	×	×	✓	✓	×	2,700 + 776	✓	✓	✓
Ablation: CoT Modalities	Qwen3-VL-4B	×	×	×	×	✓	✓	×	2,700 + 776	✓	✓	✗
ForgeryVCR*	Qwen3-VL-4B	✓	✓	✓	✓	✓	✓	✓	2,700 + 776	✓	✓	✓
ForgeryVCR (Ours)	Qwen3-VL-4B	✓	✗	✓	✓	✓	✓	✓	2,700 + 776	✓	✓	✓
Ablation: Reward Variants	Qwen3-VL-4B	✓	✗	✓	✓	Var.	Var.	Var.	2,700 + 776	✓	✓	✓
Ablation: Toolbox Variants	Qwen3-VL-4B	✓	✗	✓	✓	✓	✓	✓	2,700 + 776	✓	✓	✓

Experiment-Specific Configurations. To ensure transparency and reproducibility, we provide a detailed breakdown of the training configurations for all experiments in Table 14. Unless otherwise specified, all Supervised Fine-Tuning (SFT) stages are implemented using Low-Rank Adaptation (LoRA) with lora rank $r = 32$, lora alpha $\alpha = 64$, and a learning rate of 5e-4. The Reinforcement Learning (RL) stages are conducted with LoRA settings of $r = 128$, $\alpha = 256$, and a learning rate of 5e-5. Below, we elaborate on the specific settings for each experimental category, highlighting the differences in data strategies and optimization objectives.

- **Lightweight Tool-Specific Fine-Tuning (FT).** This preliminary stage is designed to train the single-tool expert models required for the Gain-Driven Tool Selection process. As detailed in the first row of Table 14, we employ a short training schedule of 5 epochs to prevent overfitting. Crucially, to focus on aligning visual features with forensic descriptors, we unfreeze the Vision Encoder and Projector (Aligner) while keeping the LLM backbone frozen. No complex data filtering (ISR) or synthesis (MTS) is applied here, as these models themselves serve as the filtering mechanism for subsequent stages.
- **ForgeryVCR* (Visual-Textual CoT).** This variant represents the dual-modality baseline evaluated in our main comparative results. It follows the complete two-stage training pipeline, consisting of 2,700 steps for SFT and 776 steps for RL. To support its hybrid reasoning capability, the training data is constructed using both Intractable Sample Removal (ISR) and Multi-Trajectories Synthesis (MTS), containing both visual tool tokens and detailed linguistic rationales. Consequently, the model is optimized using all three reward components (R_{cls} , R_{loc} , R_{tool}), with all modules (Vision, Aligner, and LLM) set to trainable to accommodate the complex multimodal generation.
- **ForgeryVCR (Visual-Centric Reasoning).** Our proposed Visual-Centric framework adheres to the same rigorous training schedule (2,700 SFT + 776 RL steps) and full parameter optimization (all modules trainable) as the Visual-Textual counterpart. The defining difference lies in the *CoT Modality*: we explicitly exclude intermediate linguistic descriptions from the reasoning chain, forcing the model to rely solely on visual intermediates and tool tokens. This configuration maximizes the effectiveness of the Tool Utility Reward (R_{tool}) and minimizes semantic hallucinations, serving as the standard setting for our reported state-of-the-art results.
- **Fine-tuning General MLLMs.** To benchmark against standard parameter adaptation, these baselines are fine-tuned using the identical data split and duration as ForgeryVCR. However, as they lack the forensic toolbox, they are trained without the specialized ISR/MTS strategies, using standard image-text pairs where the model directly predicts the verdict. Accordingly, the reward function during RL is modified to exclude the Tool Utility Reward (R_{tool}), focusing strictly on a weighted sum of Classification (R_{cls}) and Localization (R_{loc}) rewards.
- **Ablation: CoT Modalities.** For the “No CoT” and “Textual-Only” variants referenced in the ablation studies, we adjust the modality columns as shown in the table. Notably, for these simplified baselines, we freeze the LLM backbone and only fine-tune the Vision Encoder and Aligner to isolate the impact of reasoning modalities. Since no tools are invoked, R_{tool} is deactivated.
- **Ablation: Reward Functions.** These experiments utilize the full ForgeryVCR configuration (Visual-Centric CoT, full trainable modules) but vary the specific components like R_{cls} , R_{loc} , and R_{tool} during the RL stage to analyze the trade-offs between detection accuracy, localization precision and tool invocation strategy.
- **Ablation: Toolbox Variants.** These runs maintain the standard ForgeryVCR pipeline and optimization settings but restrict the available tool set (e.g., removing NPP or Zoom-In) during the SFT data construction and inference phases. This isolation allows us to quantify the individual contribution of each forensic component.

F. Extended Experimental Analysis

In this section, we provide supplementary experimental results covering the Reward Weight Ablation Study, Robustness against Post-Processing Degradations, Visual Mechanics of Robustness against Degradations, and Grounding Precision Analysis (BBox-IoU).

F.1. Reward Weight Ablation Study

We investigate the sensitivity of the reinforcement learning process to the hyperparameters λ_{cls} , λ_{loc} , and λ_{tool} in Eq. (5). Table 15 summarizes the performance trade-offs. We observe that increasing the localization weight λ_{loc} to 2.0 encourages better pixel-level grounding, but without a moderate penalty on tool usage ($\lambda_{tool} = 0.5$), the model may over-invoke tools, leading to slight degradation. The combination of $\{1.0, 2.0, 0.5\}$ yields the optimal balance.

F.2. Robustness against Post-Processing Degradations

To evaluate the stability of ForgeryVCR in real-world scenarios, we conducted extensive robustness tests against common image degradations. We assessed both image-level detection accuracy and pixel-level localization F1-scores under varying

Table 15. Hyperparameter sensitivity analysis on reward weights. We investigate the impact of varying λ_{cls} , λ_{loc} , and λ_{tool} on model performance. Best results are marked in **bold** and second-best are underlined. The final configuration (highlighted) achieves the optimal trade-off.

Reward Weights			Image-level Detection		Pixel-level Localization	
λ_{cls}	λ_{loc}	λ_{tool}	F1	ACC	F1	IoU
1.0	1.0	1.0	0.7920	0.7922	0.5716	0.5180
1.0	2.0	1.0	0.7883	0.7824	<u>0.5772</u>	<u>0.5230</u>
1.0	1.0	0.5	<u>0.7995</u>	<u>0.8142</u>	0.5475	0.4961
1.0	2.0	0.5	0.8271	0.8261	0.5881	0.5306

intensities of JPEG compression, Gaussian noise, Gaussian blur, and resizing operations. The comparative results against state-of-the-art specialist networks and other baselines are illustrated in Fig. 9 and 10.

It is worth noting that the visual comparisons in the aforementioned figures primarily focus on traditional IFDL methods. For MLLM-based forensic approaches such as FakeShield and SIDA, a comprehensive full-scale degradation analysis was constrained by their significantly higher complexity and inference latency. Consequently, we performed a targeted comparison with these methods specifically on the CASIA v1 dataset. Table 16 details the pixel-level localization performance (F1 and IoU) under specific degradation conditions, demonstrating that ForgeryVCR maintains superior robustness even against these multimodal counterparts.

Table 16. Quantitative robustness comparison with MLLM-based methods on CASIA v1. We report the Pixel-level Localization F1-score and IoU under JPEG compression (Quality Factors 80, 70) and Gaussian degradation (Standard Deviation 5, 10).

Method	Metric	JPEG Compression		Gaussian Noise	
		Param=80	Param=70	Param=5	Param=10
SIDA	F1	0.2774	0.2776	0.2789	0.2611
	IoU	0.2333	0.2327	0.2360	0.2195
FakeShield	F1	0.5647	0.5645	0.5494	0.5297
	IoU	0.5026	0.5022	0.4861	0.4693
ForgeryVCR	F1	0.7014	0.6973	0.7054	0.6846
	IoU	0.6771	0.6868	0.6638	0.5981

F.3. Visual Mechanics of Robustness against Degradations

As evidenced by the performance curves, ForgeryVCR consistently outperforms competing methods across all distortion types. We analyze the specific performance dynamics for each degradation category below:

To better understand the quantitative stability observed in Fig. 11, we visualize the actual outputs of our forensic tools under varying degradation intensities. We present these qualitative comparisons in Fig. 11(a) (JPEG), Fig. 11(b) (Noise), Fig. 11(c) (Blur), and Fig. 11(d) (Resizing). This inspection reveals distinct failure modes and survival mechanisms for each tool, providing a physical explanation for the performance trends.

Resilience Mechanism in JPEG Compression. Fig. 11(a) illustrates the impact of lossy compression. While the distinct high-frequency noise in the **ELA** map diminishes as the Quality Factor drops (moving left in the figure), the **structural outline** of the manipulated region (the central flower) remains faintly visible as a coherent block even at lower qualities (QF=50). **Analysis:** This visual persistence aligns with the JPEG robustness curve in Fig. 9, where our method maintains stable performance until extreme compression levels. Unlike pixel-level noise which is fragile, the *block-level* artifacts captured by ELA act as a soft indicator that degrades gracefully, allowing the MLLM to sustain localization guidance.

Vulnerability to Gaussian Noise. Contrary to the ideal scenario where forensic tools “filter out” noise, our visualization in Fig. 11(b) reveals a critical physical limitation. As the standard deviation of Gaussian noise increases beyond $\sigma = 3$, the

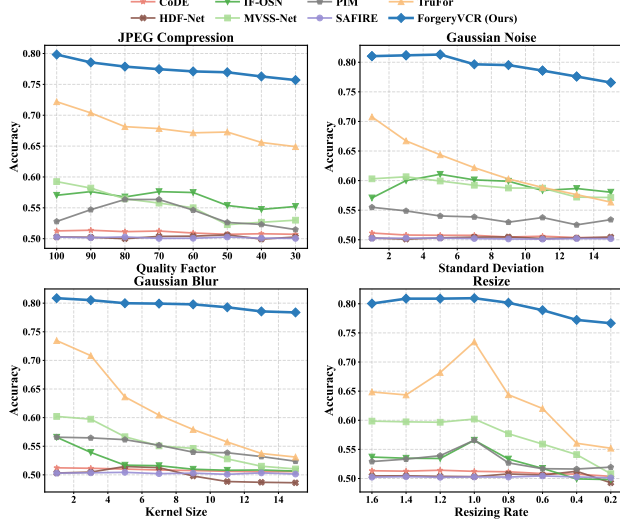


Figure 9. Detection Robustness (Accuracy). Comparison of image-level detection accuracy under varying degradation intensities. ForgeryVCR (Pink) exhibits superior stability compared to specialist networks.

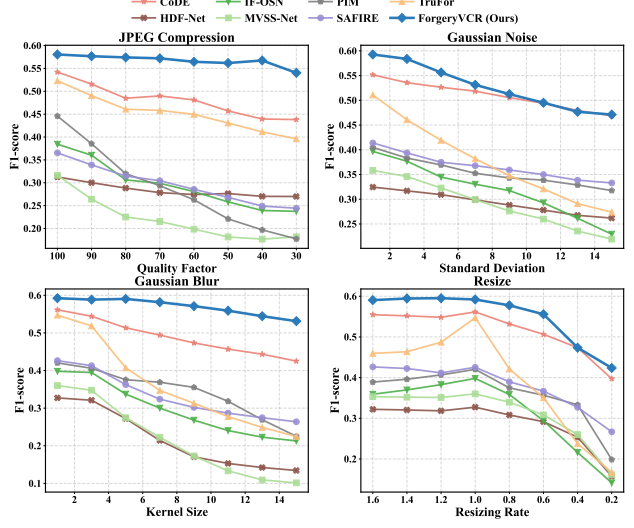


Figure 10. Localization Robustness (F1-score). Comparison of pixel-level localization F1-scores. Our framework maintains precise grounding capabilities even when high-frequency traces are attenuated.

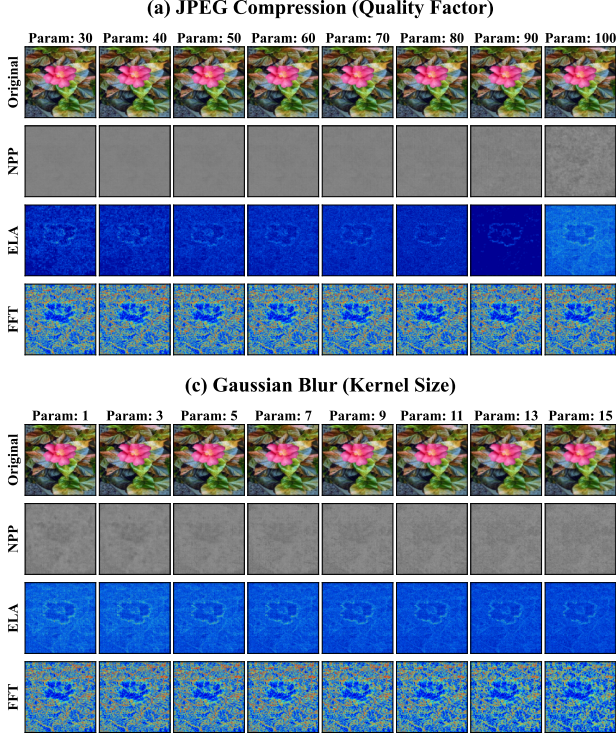


Figure 11. Robustness analysis visualization. To better understand the quantitative stability observed in the charts above, we visualize the actual outputs of our forensic tools under varying degradation intensities.

sensitive camera fingerprints relied upon by **NPP** are completely overwhelmed, turning the output into a uniform gray field. Similarly, the **ELA** map becomes dominated by global high-frequency noise.

Analysis: Despite this visual collapse of low-level features, the quantitative results in Fig. 9 show that ForgeryVCR (Pink line) maintains a high accuracy (> 0.70) even at severe noise levels ($\sigma = 14$), whereas competitors like TruFor

degrade rapidly. This discrepancy suggests that our MLLM **adaptively shifts its reasoning**. When low-level forensic tools become uninformative (as visually confirmed in Fig. 11(b)), the model pivots to high-level semantic cues (e.g., lighting inconsistencies visible in RGB) or relies on the **Zoom-In** mechanism to inspect semantic plausibility, rather than blindly trusting the corrupted forensic maps.

Behavior under Gaussian Blur. Blurring acts as a low-pass filter, detrimental to edge detection. As shown in Fig. 11(c), the sharp boundaries in the ELA map become diffuse as the kernel size increases. However, the *positional* information remains intact—the hotspot is blurred but still centered on the forgery.

Analysis: This explains why the Localization F1-score (Fig. 10) declines slowly rather than collapsing. Even if the forensic tool provides a coarse blob rather than a sharp outline, the MLLM utilizes this approximate location to attend to the region in the original image, refining the boundary via semantic segmentation to maintain reasonable performance.

Signal Amplification in Resizing. Geometric transformations introduce specific artifacts. Most notably, Fig. 11(d) reveals that **upsampling** (Rate > 1.0) actually *enhances* forensic signals: the FFT tool captures distinct periodic grid patterns, and ELA shows increased contrast.

Analysis: This visualization perfectly corroborates the unique trend observed in the Resize Accuracy curve (Fig. 9, Bottom Right). While performance drops during downsampling (Rate < 1.0) due to information loss, it recovers and even peaks during upsampling. The interpolation artifacts effectively turn the degradation into a strong detectable feature, which ForgeryVCR successfully leverages to achieve near-perfect detection in upscaled scenarios.

F.4. Grounding Precision Analysis (BBox-IoU)

While the pixel-level localization results in the main text (Table 2) demonstrate the high quality of the final segmentation masks, a potential concern is that these results might be heavily reliant on the refinement capabilities of SAM2. To decouple the contribution of the MLLM’s visual reasoning from the segmentation head, we report the **Bounding Box IoU** in Table 17.

This metric evaluates the overlap between the bounding box predicted directly by the MLLM (before SAM2 processing) and the ground truth bounding box of the manipulated region. As shown in the table, ForgeryVCR achieves superior BBox-IoU compared to baselines, confirming that our model accurately localizes forgery regions through visual-centric reasoning, providing reliable prompts for the subsequent segmentation module rather than relying on it to fix poor predictions.

Table 17. Quantitative comparison of **Bounding Box localization (BBox-IoU)**. This metric reflects the raw grounding capability of the MLLM. Best results are marked in **bold**, and second best are underlined.

Method	CASIA v1	Coverage	CocoGlide	NIST16	Korus	DSO	Columbia	In-the-wild	Weighted Avg.
MVSS-Net (<i>TPAMI’22</i>)	0.3585	0.3080	0.1850	0.2037	0.0617	0.1411	0.3920	0.1497	0.2250
IF-OSN (<i>CVPR’22</i>)	0.4439	0.0906	0.1877	0.0255	0.0668	0.0378	0.2608	0.1348	0.1560
TruFor (<i>CVPR’23</i>)	<u>0.6013</u>	<u>0.3756</u>	0.2791	0.0570	<u>0.1928</u>	0.5885	0.4946	0.2977	0.3608
CoDE (<i>TIFS’24</i>)	0.5781	0.1762	0.2723	<u>0.2841</u>	0.1478	0.1605	0.7564	0.2978	0.3341
HDF-Net (<i>TPAMI’24</i>)	0.2467	0.2050	0.1917	0.1856	0.1279	0.1453	0.4180	0.2483	0.2211
PIM (<i>TPAMI’25</i>)	0.5183	0.1944	0.4179	0.2076	0.1883	0.2515	0.5919	0.4182	0.3877
SAFIRE (<i>AAAI’25</i>)	0.1501	0.2748	0.2387	0.2191	0.1374	0.2027	0.5527	0.1877	0.2454
FakeShield (<i>ICLR’25</i>)	0.5449	0.2308	0.5323	0.2262	0.1030	0.4362	<u>0.7844</u>	<u>0.4625</u>	<u>0.4379</u>
SIDA (<i>CVPR’25</i>)	0.2936	0.2428	<u>0.5237</u>	0.1993	0.2368	0.2589	0.5806	0.4494	0.3389
ForgeryVCR	0.6962	0.6338	0.4042	0.4473	0.1856	<u>0.5524</u>	0.9267	0.6354	0.5555

G. Qualitative Visualization and Analysis

A core motivation of introducing Reinforcement Learning (RL) is to optimize the tool selection policy for both efficiency and forensic accuracy. While SFT establishes the syntactic capability to invoke tools, the model often suffers from indiscriminate tool usage, leading to reasoning paths cluttered with irrelevant or noisy feature maps. In this section, we analyze three distinct evolutionary patterns observed during the transition from SFT to RL, as visualized in Fig. 12.

Correction of Tool Selection. In the **Left column** of Fig. 12, the SFT baseline initially selects *Error Level Analysis (ELA)*. However, for this specific splicing manipulation, ELA fails to generate a distinct signal against the background,

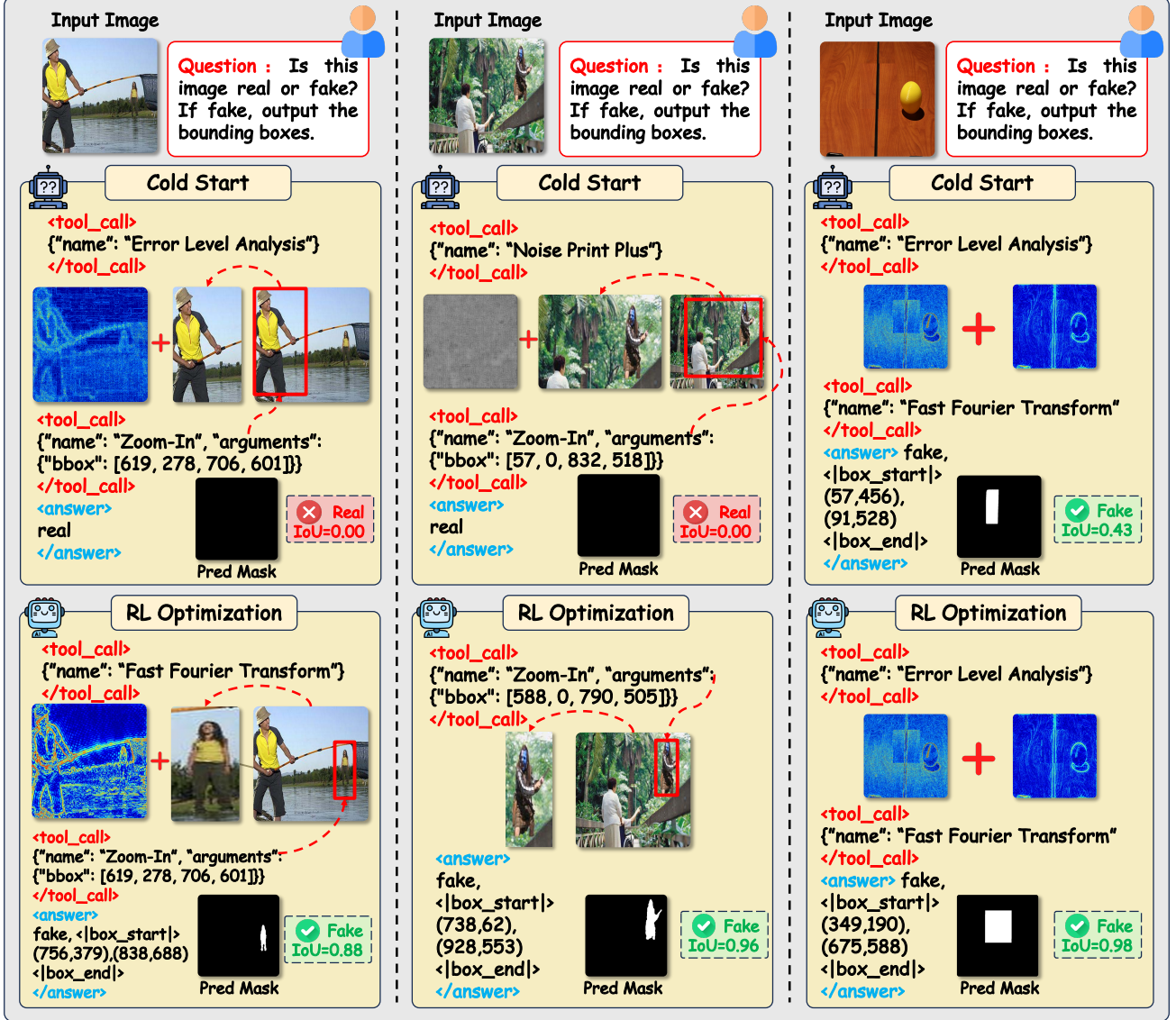


Figure 12. Qualitative comparison of policy evolution from Cold Start (SFT) to RL Optimization. The three columns illustrate distinct improvement behaviors: (Left) correcting ineffective tool selection (switching from ELA to FFT) to fix false negatives; (Middle) pruning redundant tools (removing NPP) to eliminate noise and improve efficiency; and (Right) refining spatial grounding to maximize localization precision using the same forensic cues. The face images in the left and middle figures are sourced from CASIA v1 (Dong et al., 2013); the original images are from the Corel image dataset (<http://corel.digitalriver.com/>).

resulting in a False Negative ("Real") verdict. In contrast, the RL-optimized policy successfully abandons the ineffective tool and switches to *Fast Fourier Transform (FFT)*. As seen in the generated heatmaps, the FFT visualization reveals a distinct spectral anomaly around the fisherman that was missed by ELA. This demonstrates that the MLLM has learned to strategically invoke the forensic tool that maximizes the signal-to-noise ratio for specific visual contexts, correcting the initial policy to capture valid tampering evidence (IoU 0.88).

Mitigation of Redundant Tool Invocation. The Middle column illustrates a case where "less is more." The SFT model employs a complex combination of *Noise Print Plus (NPP)* and *Zoom-In*. However, the NPP map in this specific instance appears perceptually ambiguous (a uniform gray field), which creates noise that confuses the model into an incorrect "Real" classification (IoU 0.00).

Guided by the Tool Utility Reward (R_{tool}), the RL-optimized model learns to prune this redundant step. It recognizes that

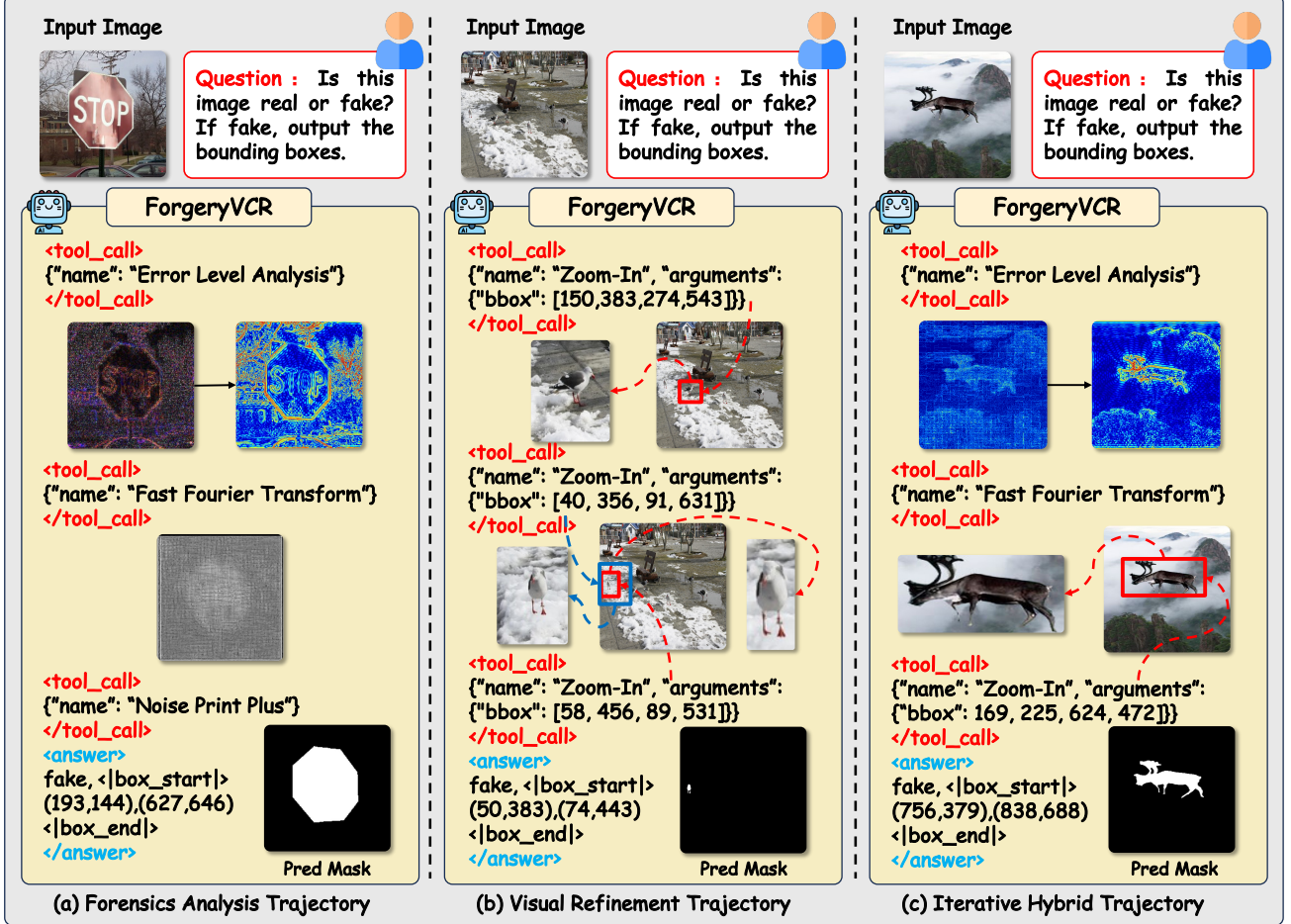


Figure 13. **Visualization of Visual-Centric Reasoning Trajectories.** We demonstrate how ForgeryVCR adaptively constructs investigation paths based on image content: (a) **Forensics Analysis Trajectory**, utilizing statistical tools like ELA, FFT, and NPP to expose hidden artifacts; (b) **Visual Refinement Trajectory**, employing the Zoom-In mechanism for multi-view fine-grained inspection; and (c) **Iterative Hybrid Trajectory**, which synergizes global forensic cues with local visual verification to generate precise localization masks.

the *Zoom-In* mechanism alone provides sufficient resolution to identify the unnatural boundaries of the spliced figures in the forest. By eliminating the interference from the unnecessary forensic filter, the MLLM not only reduces inference cost but also achieves a correct "Fake" verdict with high localization precision (IoU 0.96).

Refinement of Localization Precision. The **Right column** demonstrates the impact of the Localization Reward (R_{loc}). Here, both the SFT and RL models correctly select the same combination of tools—*Error Level Analysis* (ELA) and *Fast Fourier Transform* (FFT)—which successfully highlight the tampering traces on the wooden surface. However, the SFT model predicts a loosely defined bounding box (IoU 0.43) that includes significant background area. Driven by the pixel-level alignment objective in the RL stage, the MLLM refines its spatial reasoning. Using the identical forensic evidence, the RL-tuned model generates a much tighter bounding box (IoU 0.98) that closely hugs the contours of the manipulated object. This confirms that RL optimizes not just the *choice* of tools, but also the *interpretation* of their outputs for precise grounding.

G.1. Visual-Centric Reasoning Visualization

To intuitively understand the decision-making process of ForgeryVCR, we visualize three representative reasoning trajectories in Fig. 13. Unlike previous methods that rely on vague textual descriptions, our framework actively invokes tools to materialize imperceptible traces into explicit visual evidence.

As illustrated in Fig. 13(a), when facing invisible manipulation traces (e.g., the spliced stop sign), the model adopts the

Forensics Analysis Trajectory. It sequentially invokes *Error Level Analysis* (ELA), *Fast Fourier Transform* (FFT), and *Noise Print Plus* to reveal statistical inconsistencies that are invisible to the naked eye.

In contrast, for high-resolution images where the manipulation is small but visually discernible, Fig. 13(b) shows the Visual Refinement Trajectory. Here, the model bypasses global forensic tools and instead continuously triggers the Zoom-In tool to inspect the suspicious bird regions, progressively narrowing down the bounding box for exact localization.

Finally, Fig. 13(c) presents the Iterative Hybrid Trajectory, which handles the most complex scenarios. The model first detects spectral anomalies using forensic analysis tools like ELA and FFT, and then verifies by zooming in on the specific region (the deer). This combination ensures that the final prediction is grounded in both statistical and semantic evidence.

G.2. Qualitative Comparison with SOTA Methods

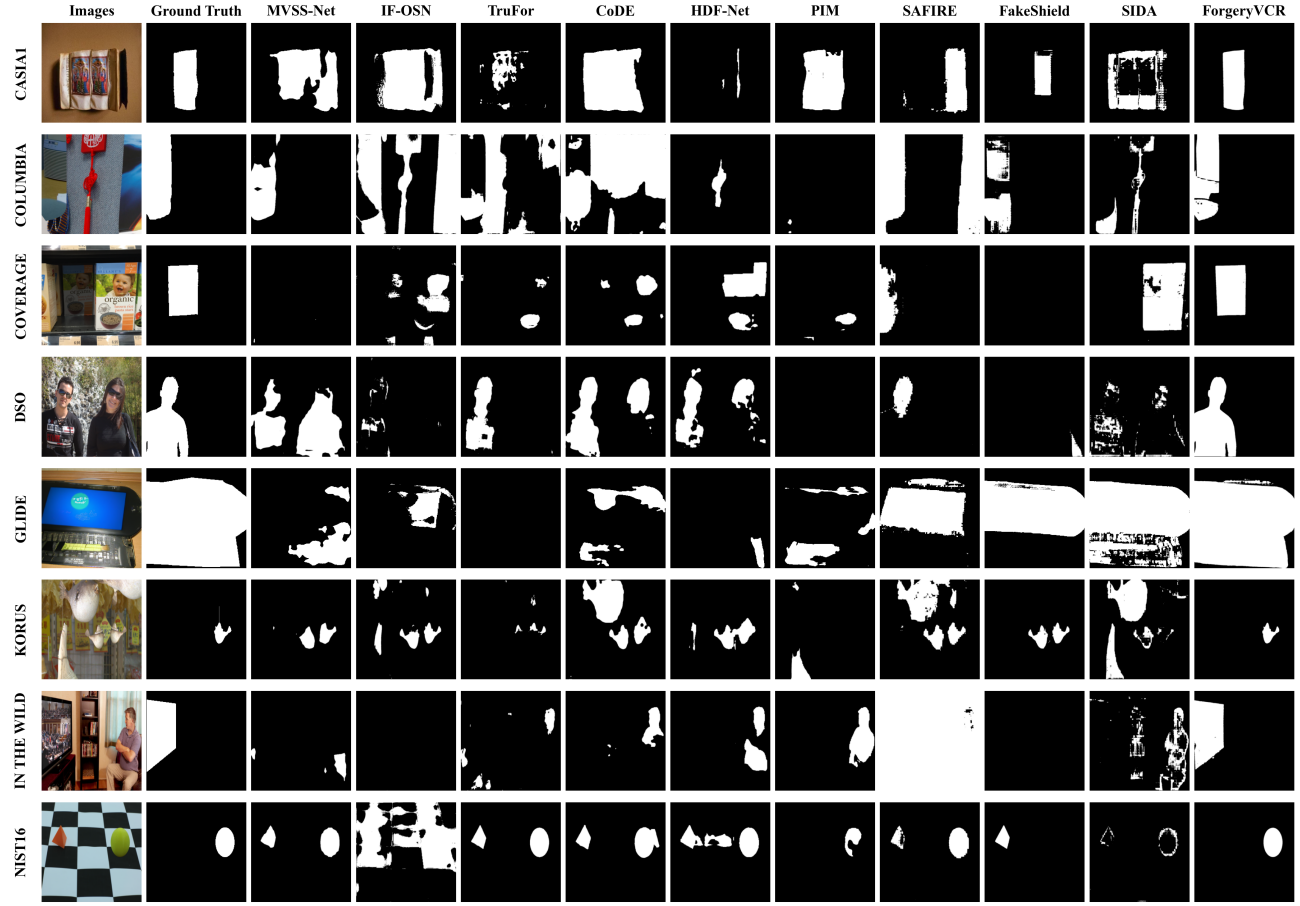


Figure 14. Qualitative comparison of pixel-level localization masks across benchmark datasets. We compare ForgeryVCR with representative baselines including specialist networks and forensic-tuned MLLMs. Our method consistently produces high-fidelity masks that closely align with the Ground Truth (GT), effectively suppressing background noise and accurately delineating manipulated boundaries. Original images source of DSO datasets (De Carvalho et al., 2013) is Flickr (www.flickr.com).

To visually substantiate the quantitative localization performance reported in the main text, we provide a comprehensive comparison of predicted manipulation masks against state-of-the-art competitors in Fig. 14. The visualization spans diverse benchmarks, covering challenges such as copy-move, splicing, and complex in-the-wild manipulations. As observed in the figure, traditional deep forensic networks often struggle with background noise, producing fragmented masks with high false-positive rates. In contrast, ForgeryVCR leverages high-level semantic reasoning to filter out irrelevant texture variations, resulting in cleaner binary masks. Furthermore, compared to other MLLM-based methods that tend to generate coarse regions, our approach achieves superior boundary adherence by effectively synergizing the MLLM’s spatial reasoning with the fine-grained segmentation capability of SAM 2.

H. Prompt Templates

H.1. System Configuration and User Query Templates

System Prompt Template

You are a helpful assistant.

Tools

You may call one or more functions to assist with the user query.

You are provided with function signatures within <tools></tools> XML tags:

```

<tools>
[
{
  "type": "function",
  "function": {
    "name": "zoom_in",
    "description": "Zooms in on a suspicious region to check for fine-grained manipulation artifacts like inconsistent textures or noise.",
    "parameters": {
      "type": "object",
      "properties": {
        "bbox": {
          "type": "array",
          "items": {"type": "integer"},
          "description": "The bounding box coordinates [x1, y1, x2, y2] of the region to zoom in."
        }
      },
      "required": ["bbox"]
    }
  }
},
{
  "type": "function",
  "function": {
    "name": "ELA",
    "description": "Performs Error Level Analysis to reveal inconsistencies in the image's compression levels. Tampered regions often exhibit distinct error levels.",
    "parameters": {
      "type": "object",
      "properties": {},
      "required": []
    }
  }
},
{
  "type": "function",
  "function": {
    "name": "FFT",
    "description": "Analyzes the image's frequency domain using Fast Fourier Transform. Tampering can introduce periodic artifacts or disrupt natural frequency patterns.",
    "parameters": {

```

System Prompt Template (Continued)

```

    "type": "object",
    "properties": {},
    "required": []
}
},
{
    "type": "function",
    "function": {
        "name": "NPP",
        "description": "Analyzes the image's noise fingerprints using Noise Print Pattern. Tampered regions often show inconsistent noise variance compared to the authentic background.",
        "parameters": {
            "type": "object",
            "properties": {},
            "required": []
        }
    }
}
]
</tools>

```

For each function call, return a json object with function name and arguments within `<tool_call></tool_call>` XML tags:

```

<tool_call>
{"name": <function-name>, "arguments": <args-json-object>}
</tool_call>

```

User Prompt Template

`<image>`Determine if this image is real or fake. If manipulation is found, highlight the tampered regions with bounding boxes.

H.2. Trajectory Synthesis Templates for CoT Data Generation**Prompt Template 1: No-Tool Direct Assessment**

[BEGIN OF GOAL]

You are an expert visual assistant specializing in digital image forensics. Your goal is to generate a plausible step-by-step reasoning trajectory to identify tampered regions within an image. The trajectory should be presented as a single-turn dialogue between a “User” and an “Assistant”, where the Assistant performs a comprehensive visual analysis and provides a final conclusion without the need for external tools.

[END OF GOAL]

[BEGIN OF ACTIONS]

Name: Terminate

Description: Concludes the analysis and provides the final answer. This action must be called at the end of the trajectory.

Examples:

Tool Called: Terminate

Prompt Template 1: (Continued)

[END OF ACTIONS]

[BEGIN OF TASK INSTRUCTIONS]

You are given two images: the original image and a ground truth overlay showing the exact tampered region. The overlay is your absolute source of truth for your conclusion.

Your task is to generate a single-round dialogue.

1. The “User” will ask for an analysis.
2. Your “Assistant” response must be a comprehensive analysis of the original image.
3. Your reasoning MUST focus on the specific object highlighted in the ground truth overlay. Describe visual inconsistencies on that object (e.g., unnatural texture, mismatched lighting, sharp edges, incorrect shadows).
4. Your speech must conclude with a precise final verdict, accurately identifying the tampered object and describing its location textually (e.g., “in the bottom-left corner”, “on top of the building”).
5. Finally, call the “Terminate” action.
6. **Crucially, your entire output must not mention the ground truth overlay or refer to images by number (e.g., [Image 2]). You are simulating an expert’s direct analysis.**
7. **Your final verdict MUST NOT contain any bounding box coordinates or the “<bbox>” placeholder.**

[END OF TASK INSTRUCTIONS]

[BEGIN OF OUTPUT FORMAT]

Your output must be a single block starting with “[BEGIN OF SOLUTION]” and ending with “[END OF SOLUTION]”. The dialogue must be in a single round.

[BEGIN OF SOLUTION]

Round 1

User: “Please analyze the provided image for any signs of tampering. If you find any, explain why and identify the manipulated areas. If not, please confirm its authenticity and describe your analysis.”

Assistant: “[Your detailed analysis and final verdict here]”

Tool Called: Terminate

[END OF SOLUTION]

[END OF OUTPUT FORMAT]

[BEGIN OF EXAMPLES]

[BEGIN OF SOLUTION]

Round 1

User: “Please analyze the provided image for any signs of tampering. If you find any, explain why and identify the manipulated areas. If not, please confirm its authenticity and describe your analysis.”

Assistant: “I am analyzing a photograph showing a group of monkeys on a stone wall. Upon close inspection, the monkey located in the bottom-left corner exhibits clear signs of digital manipulation. Its internal texture is unnaturally smooth and lacks the fine fur detail present on the other monkeys. Furthermore, the lighting on this monkey is flat and inconsistent with the ambient light of the scene, and it casts no discernible shadow on the wall beneath it. My analysis is complete. The image is tampered, and the manipulated object is the monkey in the bottom-left of the image.”

Tool Called: Terminate

[END OF SOLUTION]

[END OF EXAMPLES]

Prompt Template 2: Single-Tool Analysis (e.g., ELA)

[BEGIN OF GOAL]

You are an expert visual assistant specializing in digital image forensics. Your goal is to generate a plausible step-by-step reasoning trajectory to identify tampered regions within an image. The core of your analysis depends on identifying **inconsistencies** rather than just visual anomalies. The final output should be a multi-turn dialogue between

Prompt Template 2: (Continued)

a “User” and an “Assistant”.

[END OF GOAL]

[BEGIN OF ACTIONS]

Name: ELA

Description: Generates an Error Level Analysis (ELA) heatmap to reveal discrepancies in compression history.

Crucially, do not assume that bright areas are automatically tampered.

* **Normal Behavior:** Areas with complex textures (e.g., foliage, gravel, fur) naturally exhibit higher error levels (brighter noise) in ELA. Smooth areas (e.g., sky, skin) usually appear dark.

* **Tampering Indicators:** Look for **mismatches**. A tampered region often breaks the continuity of the noise pattern. For example, a visually smooth object appearing suspiciously bright in ELA, or an object exhibiting a distinct noise texture (e.g., different color distribution or density) that does not match the surrounding environment’s error profile.

Name: Terminate

Description: Concludes the analysis and provides the final answer. This action must be called at the end of every trajectory.

[END OF ACTIONS]

[BEGIN OF TASK INSTRUCTIONS]

You are given three images: the original image, the ground truth overlay (your absolute source of truth), and an ELA heatmap.

Your task is to generate a two-round dialogue.

1. **Round 1:** The “Assistant” analyzes the **original image only**. Focus on the object highlighted in the ground truth. Describe visual suspicions regarding **consistency**: Does the object’s lighting, resolution, or grain match its surroundings? (e.g., “The object seems to have a different texture quality compared to the background”). Conclude by calling “ELA”.

2. **Round 2:** The “Assistant” analyzes the **ELA heatmap**.

* **Contextual Comparison:** Compare the suspicious area’s ELA signature against the rest of the image.

* **Reasoning:** Explain *why* the ELA pattern is suspicious. Is it brighter than it *should* be given its visual texture? Does the noise pattern look “pasted” on top of the background noise?

* **Avoid False Positives:** Acknowledge that natural textures are noisy, but highlight that the tampered object has a *distinct* or *alien* noise profile compared to valid high-frequency areas.

* Integrate findings to form a conclusion and call “Terminate”.

3. **Crucially, do not mention the ground truth overlay or refer to images by number.**

4. **Your final verdict MUST NOT contain any bounding box coordinates or the “<bbox>” placeholder.**

[END OF TASK INSTRUCTIONS]

[BEGIN OF OUTPUT FORMAT]

Your output must be a single block starting with “[BEGIN OF SOLUTION]” and ending with “[END OF SOLUTION]”. The dialogue must be in two rounds.

[BEGIN OF SOLUTION]

Round 1

User: “Is this image authentic? Leave no stone unturned.”

Assistant: “[Analysis of the original image, focusing on visual inconsistencies like lighting or edge artifacts]”

Tool Called: ELA

Round 2

Assistant: “[Analysis of the ELA heatmap. Explicitly discusses the “mismatch” between visual texture and error level. Conclusion describes the tampered object]”

Tool Called: Terminate

[END OF SOLUTION]

Prompt Template 2: (Continued)

[END OF OUTPUT FORMAT]

[BEGIN OF EXAMPLES]

[BEGIN OF SOLUTION]

Round 1

User: "Is this image authentic? Leave no stone unturned."

Assistant: "I am examining an image of a grassy field with a zebra standing in the center. While the scene looks mostly natural, I notice the zebra's outline seems slightly too sharp against the background grass, and the lighting on its coat doesn't perfectly match the ambient direction. This raises a suspicion that the zebra might have been inserted. I will use ELA to check for compression inconsistencies."

Tool Called: ELA

Round 2

Assistant: "Analyzing the ELA heatmap, I see significant noise across the entire image, which is expected given the complex texture of the grass. However, the area corresponding to the zebra exhibits a **distinctly different noise intensity and color distribution** compared to the surrounding grass. While the grass shows a uniform high-frequency scatter, the zebra stands out as a solid block of hyper-intense artifacts that doesn't blend with the environment's noise profile. This **inconsistency in error levels** confirms that the zebra originates from a different source and was pasted into this scene. The image is tampered."

Tool Called: Terminate

[END OF SOLUTION]

[END OF EXAMPLES]

Prompt Template 3: Multi-Tool Synthesis

[BEGIN OF GOAL]

You are an expert visual assistant specializing in digital image forensics. Your goal is to generate a plausible step-by-step reasoning trajectory to identify a **fake** (manipulated) object within an image. You will conduct a comprehensive forensic investigation using visual analysis and three specialized tools (**{t1}**, **{t2}**, and **{t3}**) to build an unshakeable chain of evidence.

[END OF GOAL]

[BEGIN OF ACTIONS]

Name: NPP

Description: Analyzes noise patterns. Fakes appear as disrupted noise fingerprints.

Name: ELA

Description: ELA Heatmap. Fakes appear as compression anomalies (unexplained brightness).

Name: FFT

Description: High-Frequency Energy Map. Fakes appear as frequency mismatches (color contrast islands).

Name: Terminate

Description: Concludes the analysis. Must be called at the end.

[END OF ACTIONS]

[BEGIN OF TASK INSTRUCTIONS]

You are given four inputs:

1. The **Original Image**.
2. The **Ground Truth Overlay** (This is your SECRET source of truth. It highlights the exact manipulated region).
3. The **{t1} Map**.
4. The **{t2} Map**.
5. The **{t3} Map**.

Your task is to generate a **four-round dialogue** to expose the forgery.

Prompt Template 3: Multi-Tool Synthesis (Continued)

CRITICAL RULE: You must NEVER mention the “Ground Truth Overlay” or “Mask” in your output. You must pretend you discovered the suspicious area through your own visual and forensic analysis.

1. Round 1 (Visual Suspicion):

- * **Internal Step:** Look at the Ground Truth Overlay to identify the specific object/region.
- * **External Output:** Analyze the **Original Image**. Focus your “suspicion” on that specific object. Describe visual inconsistencies (e.g., lighting, sharpness, grain).
- * **Action:** Call “{t1}”.

2. Round 2 (First Verification - {t1}):

- * Analyze the **{t1} Map** focusing on the suspicious object.
- * **Analysis Guide:**
 {t1_guide}
- * **Requirement:** Describe the anomaly (e.g., “The map shows a distinct [feature] on the [object]...”).
- * **Creative Transition:** State that this is a strong indicator of manipulation. Generate a **diverse transitional phrase** to introduce the next tool.
 - * **Instruction:** **Avoid repetitive phrasing.** (e.g., “To investigate this inconsistency further...”, “Checking the spectral/compression domain with...”, “Let’s cross-reference this artifact...”).
 - * **Action:** Call “{t2}”.

3. Round 3 (Second Verification - {t2}):

- * Analyze the **{t2} Map** focusing on the same object.
- * **Analysis Guide:**
 {t2_guide}
- * **Requirement:** Confirm the anomaly persists in this domain as well. Describe the specific heatmap/noise features.
- * **Creative Transition:** Generate a **varied closing transition** to the final tool.
 - * **Instruction:** **Be creative.** (e.g., “For a definitive conclusion...”, “To close the evidentiary loop...”, “One final verification to confirm the forgery...”).
 - * **Action:** Call “{t3}”.

4. Round 4 (Final Verification - {t3} & Verdict):

- * Analyze the **{t3} Map** focusing on the same object.
- * **Analysis Guide:**
 {t3_guide}
- * **Requirement:** Confirm that {t3} also highlights the same object as anomalous.
- * **Verdict:** Synthesize all evidences. State clearly: “The image is fake.” Provide a final descriptive verdict identifying the **object** and its **location** (e.g., “The image is fake, and the manipulated object is the car on the left”).
- * **Action:** Call “Terminate”.

5. Formatting: Do not refer to images by number. Simulate a professional workflow.

[END OF TASK INSTRUCTIONS]

[BEGIN OF OUTPUT FORMAT]

Your output must be a single block starting with “[BEGIN OF SOLUTION]” and ending with “[END OF SOLUTION]”.

[BEGIN OF SOLUTION]

Round 1

User: “Is this image real? Leave no stone unturned.”

Assistant: “[Visual analysis raising suspicion about the specific object found in the overlay...]”

Tool Called: {t1}

Round 2

Assistant: “[Analysis of {t1} showing anomaly... Varied transition to {t2}]”

Prompt Template 3: Multi-Tool Synthesis (Continued)

Tool Called: {t2}

Round 3

Assistant: “[Analysis of {t2} showing anomaly... Varied transition to {t3}]”

Tool Called: {t3}

Round 4

Assistant: “[Analysis of {t3} showing anomaly... Final Descriptive Verdict: The image is fake...]”

Tool Called: Terminate

[END OF SOLUTION]

[END OF OUTPUT FORMAT]